# Mesoscale differences in brain organization in schizophrenia revealed by topological data analysis

**Emil Dmitruk[1], Christoph Metzner[2,3], Volker Steuber[1], Shabnam N. Kadir[1]**

[1] *Biocomputation Research Group, Department of Computer Science, University of Hertfordshire, Hatfield, United Kingdom*
[2] *Institute of Software Engineering and Theoretical Computer Science, Technische Universität Berlin, Germany*
[3] *Department of Child and Adolescent Psychiatry, Charité – Universitätsmedizin Berlin, Berlin, Germany*

June 20, 2025

**Abstract**

We uncover a novel, mesoscale perspective of the differences in the white-matter connectome between healthy controls (HC) and subjects with schizophrenia (SCH) using a method developed from computational algebraic topology: persistent homology (PH) via clique topology. We extract and compare topological motifs found in the structural connectomes of the subjects in the two groups and find significant differences. We compare our results with those obtained from easy-to-interpret null models to build an understanding of the connectivity patterns found in the data, and we explore the overlap of mesoscale structures found in two different datasets, *COBRE* (Center of Biomedical Research Excellence) and *HCP* (Human Connectome Project). Differences in acquisition usually render experiments recorded on different scanners incomparable, but here we see that there are shared structures. Our method offers a way to establish connectomic fingerprinting that could lead to a neuroimaging-based diagnosis of schizophrenia and other psychiatric and neurological conditions as well as the development of new treatments.

# 1 Introduction

Schizophrenia is a severe and chronic mental disorder that significantly affects how an individual thinks, feels, and behaves. It has a wide range of symptoms, ranging from psychosis, hallucinations and delusions, to disturbances in cognition. Despite decades of research, the causes are still unclear [Howes et al., 2023, Shen et al., 2023].

White matter deterioration is recognised as a key contributor to the pathophysiology of schizophrenia [Konrad and Winterer, 2007, Ellison-Wright and Bullmore, 2009]. While recent reviews have reported alterations across entire fibre tracts [Vitolo et al., 2017, Male et al., 2024], these findings often lack specificity regarding which tract components are affected—an important limitation given that individual tracts can span numerous brain regions. To address this, we introduce a topological framework that identifies candidate connectivity patterns, indicating how and between which regions the white-matter connectivity is altered.

Studies of schizophrenia typically focus either on global brain measures (e.g., overall cortical folding [Sasabayashi et al., 2021, Rosa et al., 2021, Kuo and Pogue-Geile, 2019]) or on local changes in specific brain areas (e.g. cortical thickness [van Erp et al., 2018] or grey matter volume [Kuo and Pogue-Geile, 2019]). It is thought that alterations in the brain's structural connectivity, or 'structural connectome,' may play an important role in schizophrenia. Notably, schizophrenia is associated with degeneration in the white-matter connectome (as evidenced in [Fornito et al., 2011, Zalesky et al., 2011, Repple et al., 2023]).

Studies of the connectome, particularly those using graph theory, tend to be node-centric or edge-centric, (e.g. graph-theory measures of the degree distribution, clustering coefficient, characteristic path length, [Stam and Reijneveld, 2007], rich club coefficient [van den Heuvel et al., 2013, Van Den Heuvel and Sporns, 2019], small-worldness [Rubinov and Sporns, 2010, Sporns, 2013], edge functional connectivity [Faskowitz et al., 2020, Faskowitz et al., 2022], centrality, average and modal controllability [Dimulescu et al., 2021]). However, these metrics are fundamentally limited to pairwise interactions and overlook higher-order relationships among brain regions.

Recently, topological data analysis (TDA), an approach from computational algebraic topology that inherently considers information from not only nodes and edges but also structures of all possible higher dimensions, has gained attention in neuroscience. TDA allows for the characterisation of higher-order relations and the identification and quantification of more complex interrelationships between multiple brain areas. While some studies focused on building a general understanding of the topology of functional connectivity [Singh et al., 2008, Ellis and Klein, 2014, Lord et al., 2016, Phinyomark et al., 2017, Anderson et al., 2018, Ellis et al., 2019, Caputi et al., 2021], others have specifically examined how functional brain connectivity is altered in brain degenerative diseases and psychiatric disorders, such as ADHD [Lee et al., 2011, Ellis and Klein, 2014], Parkinson's disease [Zhang et al., 2023], schizophrenia [Stolz et al., 2017, Stolz et al., 2018, Caputi et al., 2021, Alexander-Bloch et al., 2013, Hadley et al., 2016] or early psychosis [Fournier et al., 2020]. So far, structural connectivity has only been studied in healthy subjects [Sizemore et al., 2018], leaving its role in brain disorders unexplored.

In this present study, we explore the structural white-matter connectome using methods of topological data analysis on neuroimaging data. We uncover both specific differences in mesoscale-level brain structure as well as similarities between the subjects with schizophrenia (SCH) and healthy controls (HC). We derive structural networks of brain regions from DTI and T1-weighted MRI images in the *COBRE* dataset by computing persistent homology obtained from the order complex derived from the white matter connectivity matrix. Through this process, we measure topological features reflecting the organisation of cliques in a person's connectome and obtain the mesoscale-level brain structures [Betzel and Bassett, 2018], described by persistent homology classes of cycles. These topological structures can be grouped by dimension depending on whether they correspond to clusters, holes, hollow voids, etc.

A key insight that our method of analysis provides is that the relative prominence of different mesoscale structures within a connectome is important. For instance, although a handful of brain areas might be connected in very much the same way with a similar number of connections, for both a schizophrenia patient and a healthy subject, resulting in a near identical appearance on neuroimaging scans, relative to other structural connections in the individual's brain, this set of identical connections could rank very differently. It could be significantly stronger or weaker, so it could either dominate or be drowned out by activity in the other regions. These relative differences can be detected in the 'persistence

landscapes', and we find significant differences between schizophrenia patients and healthy controls. Therefore, sub-networks of the brain that appear to look nearly identical in the two groups under some neuroimaging protocol, may nevertheless be more dominant in one group than another, thereby causing differences in behaviour and symptoms of disease.

Lastly, we demonstrate that our approach is robust to differences in scanning equipment - the majority of the most prominent mesoscale structures were shared between healthy subjects from the *HCP* dataset [Van Essen et al., 2012] and the *COBRE* dataset, enabling comparison across datasets.

Our approach is a first step towards the development of neuroimaging biomarkers for psychiatric and neurological conditions such as schizophrenia.

# 2 Methods and Materials

We used two datasets:(1) Centre for Biomedical Research Excellence (*COBRE*) dataset (fcon_1000.projects.nitrc.org/indi/retro/cobre.html), (2) Human Connectome Project (*HCP* dataset, humanconnectome.org).

## 2.1 Data sets

### 2.1.1 *COBRE* dataset

The *COBRE* data set [Aine et al., 2017, Cetin et al., 2014] consists of structural magnetic resonance imaging scans of healthy controls (HC) ($N = 44$, 11 female) and schizophrenia patients (SCH) ($N = 44$). Data were obtained by querying the SchizConnect database (http://schizconnect.org). The HC group were matched by age and sex to the SCH group as in [Dimulescu et al., 2021].

Table 1: Illness information. The *COBRE* dataset comes with the evaluation of the state of SCH patients done with a Positive and Negative Affect Schedule (PANSS) scale [Zevon and Tellegen, 1982, Watson et al., 1988].

| | Mean (± std. dev.) | Min | Max |
|---|---|---|---|
| Age | 38.30(±13.96) | 19 | 65 |
| Age illness onset | 21.33(±7.04) | 12 | 47 |
| Illness duration | 16.96(±13.14) | 1 | 41 |
| Medication- CPZ equivalent dose | 373.52(±331.86) | 25 | 1800 |
| PANSS- Positive | 14.34(±4.99) | 7 | 28 |
| PANSS- Negative | 14.45(±4.96) | 8 | 29 |
| PANSS- Gen. Psychosomatic | 28.48(±8.26) | 16 | 56 |

Data was collected on a Siemens Magnetom Trio 3T MR device with the acquisition parameters presented in Table 2. This study used diffusion-weighted tensor image (DWI) data and high-resolution T1-weighted images; details of data acquisition and initial data preprocessing are outlined in detail in [Dimulescu et al., 2021, Cetin et al., 2014].

Table 2: Acquisition parameters for structural and diffusion tensor imaging for *COBRE* and *HCP* datasets.

| | Structural images (T1-weighted) | | Diffusion tensor imaging (DTI) | |
|---|---|---|---|---|
| | *COBRE* | *HCP* | *COBRE* | *HCP* |
| Repetition time (TR) | 2530 ms | 2400 ms | 9000 ms | 5520 ms |
| Echo time (TE) | 1.64, 3.5, 5.36, 7.22, 9.08 ms | 2.14 ms | 84 ms | 89.50 ms |
| TR/TE | - | - | 9000/84 ms | 5520/89 ms |
| Inversion time (TI) | 1200 ms | 1000 ms | - | - |
| Flip angle (FA) | 7° | 8° | 90° | 78° |
| Field of view (FOV) | 256 mm × 256 mm | 224 mm × 224 mm | 256 mm × 256 mm | 210 mm × 210 mm |
| Matrix | 256 mm × 256 mm | - | 128 mm × 128 mm | - |
| Voxel size | $1.0mm \times 1.0mm \times 1.0mm$ | $0.7mm \times 0.7mm \times 0.7mm$ | $2.00mm \times 2.00mm \times 2.00mm$ | $1.25mm \times 1.25mm \times 1.25mm$ |
| Slice thickness | 1 mm | 0.7 mm | 2 mm | 1.25 mm |
| Total slices (direction) | 192 (sagittal) | 320 (sagittal) | 74 (axial) | 111 |
| Additional parameters | - | - | 30 non-collinear diffusion gradients (b = 800 s/mm$^2$) and 5 non-diffusion-weighted images (b = 0 s/mm$^2$) equally interspersed between the 30 gradient directions | Each of the gradient tables includes approximately 90 diffusion weighting directions plus 6 b=0 acquisitions interspersed throughout each run. Diffusion weighting consisted of 3 shells of b=1000, 2000, and 3000 $s/mm^2$ interspersed with an approximately equal number of acquisitions on each shell within each run |

### 2.1.2 Human Connectome Project.

Data from 88 healthy subjects (33 female) from the Human Connectome Project [Van Essen et al., 2012] were used (the size matched the number of subjects in the *COBRE* dataset). It was not possible to match subjects according to age as only 13 out of 1133 *HCP* subjects were over 36, while the average age for COBRE subjects is 38.3 years.

A modified Siemens Skyra 3T MRI scanner was used [Sotiropoulos et al., 2013], and the acquisition parameters are presented in Table 2. We refer the reader to [Van Essen et al., 2012] for full details.

## 2.2 Data preparation/processing

### 2.2.1 Computing brain connectivity matrix

T1-weighted and DTI images were preprocessed with a semi-automatic pipeline from the *FSL* toolbox [Smith et al., 2004, Jenkinson et al., 2012](fsl.fmrib.ox.ac.uk). For the T1 images, this involved the following steps: removal of non-brain tissue, brain extraction, brain mask generation, and brain parcellation according to the AAL2 atlas [Rolls et al., 2015]. Brain extraction was applied to the DTI data, followed by head movement corrections and the removal of eddy current distortions. The probabilistic diffusion model was fit to the data with Bayesian Estimation of Diffusion Parameters Obtained using Sampling Techniques (BEDPOSTX) [Hernández et al., 2013] *FSL* toolbox.

Subjects' DTI images were linearly registered to their corresponding anatomical T1 images; the anatomical high-resolution masks were transformed into the subjects' diffusion space, and this was followed by running probabilistic tractography with 5000 samples per voxel using the PROBTRACKX algorithm [Behrens et al., 2007]. The output of this pipeline is a $94 \times 94$ structural connectivity matrix $M$. The elements of this matrix, $M_{ij}$, describe the estimated number of connections from brain region $i$ to region $j$ from the AAL2 atlas, which has 94 distinct brain regions (see Supplementary Table 65).

### 2.2.2 Symmetrizing and ordering brain region connectivity.

The topological features are obtained from the structural connectivity of each subject. This involves three steps described below: (1) computing the connectivity for every pair of regions, (2) ordering/ranking the matrix entries, and (3) running weighted-rank clique filtration on the ordered matrix.

**Symmetrizing brain region connectivity.** In general, a probabilistic fibre-tracking algorithm results in a non-symmetric matrix, $M$, describing the probability of two regions being connected, i.e., the probability of a path from region $i$ to region $j$ is not the same as that of a path from region $j$ to region $i$ [Fornito et al., 2016]. However, these matrices are very nearly symmetric (see Figure 1), which justifies our approach of building undirected simplicial complexes instead of directed flag complexes for our analysis. A symmetrized connectivity matrix $\overline{M}$ is obtained from $M$ the usual way: $\overline{M}_{i,j} = \overline{M}_{j,i} = (M_{i,j} + M_{j,i})/2$.

**Ordered matrix of brain region connectivity.** The order matrix $\hat{O}$ is a symmetric matrix of positive integers obtained by replacing the above (or below) diagonal entries of the symmetric matrix $\overline{M}$ by their ranking from the largest to the smallest (or vice versa):

$$\hat{O}_{i,j} = \hat{O}_{j,i} = ord(\overline{M}_{i,j}) \tag{1}$$

The strongest connection from $\overline{M}$ in $\hat{O}$ is numbered 1, the second strongest 2, etc (see Figure 2 for an example).

## 2.3 Persistent homology

PH is a topological data analysis method that studies the 'shape of data' at various scales. At the core of persistent homology is the idea of homology groups, which are key topological features of a space. Precise details of the tools (e.g. homology, persistent homology, simplicial complexes, frequency scaffolds) from algebraic topology that we are using are presented in Supplementary Methods Section A.2. Here we outline the main ideas and intuition. Further rigorous mathematical definitions can be found in [Giusti et al., 2015b, Otter et al., 2017, Stolz et al., 2018, Bubenik and Dłotko, 2017]).

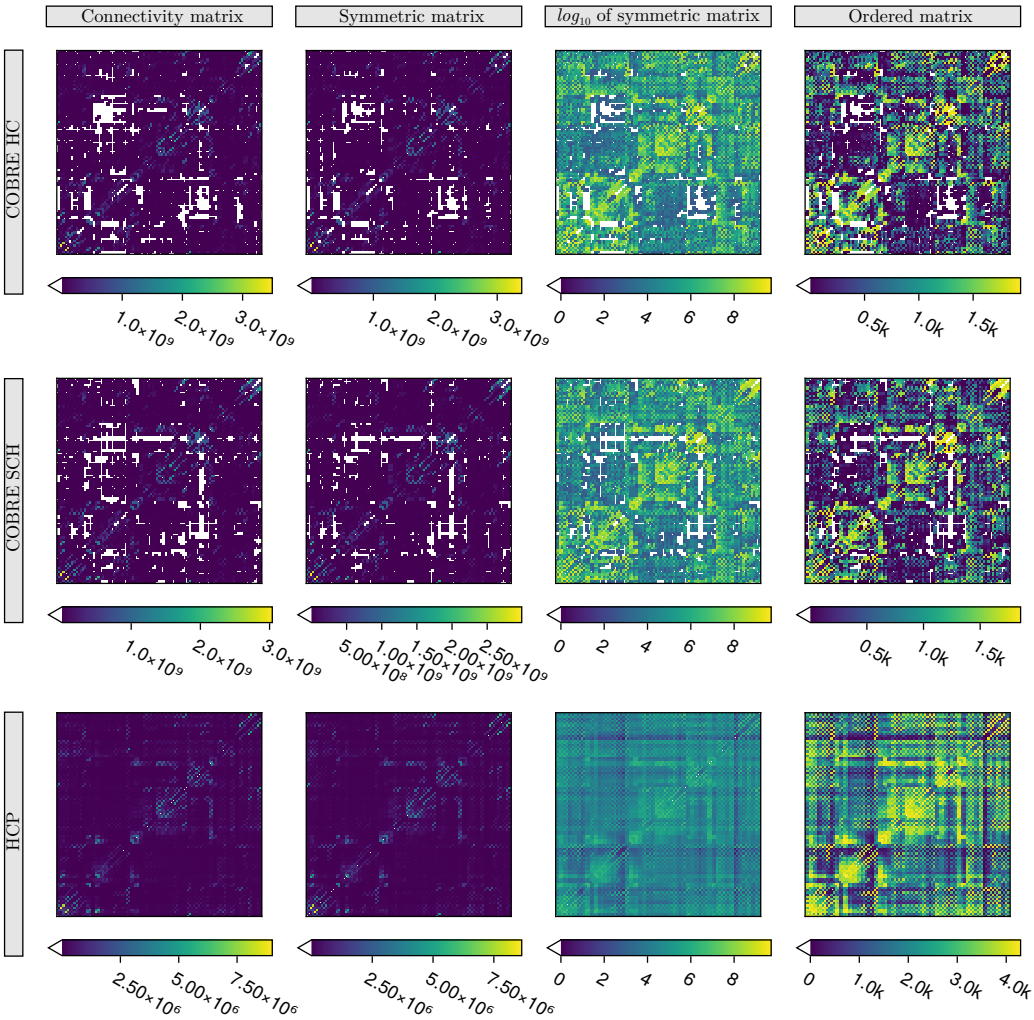


Figure 1: Heatmaps of sample matrices from the *COBRE* dataset (*HC* in the top row, *SCH* in the middle row) and *HCP* dataset (in the bottom row). The first column presents connectivity matrices obtained from probabilistic fibre tracking; the second corresponds to the symmetrised matrix; the third demonstrates the result of non-linear-transformation of the symmetrised matrix ($log_{10}$); the fourth corresponds to the ordered matrix. In each plot (except non-linear transformation), colours are fitted on a different range of values.

**Simplicial complexes** The structures we work with are simplicial complexes derived from the DTI-data. The building blocks of simplicial complexes are called $n$-simplices, where $n$ denotes the dimension of the building block. As shown in Figure 2, a $0-simplex$ is a node, a $1-simplex$ is an edge, as is the case in graph theory. TDA goes beyond this and also works with higher-dimensional structures conveying multi-connectivity; so a $2-simplex$ is formed from 3 connected nodes forming a triangle; a $3-simplex$ is formed from 4 all-to-all connected nodes (or clique), etc. In general, an $n$-simplex corresponds to a clique with $(n+1)$ nodes. Every subclique of a clique is a lower-dimensional clique.

A simplicial complex $K$ is a finite collection of simplices. If a simplex $\sigma \in K$, and $\sigma' \leq \sigma$, it implies that $\sigma' \in K$ (here we use $\leq$ to denote 'subset of'). Also, if $\sigma$ and $\sigma'$ are two simplexes of $K$, their intersection is either empty or a common face of $\sigma$ and $\sigma'$.

Homology assesses the existence of features such as connected components, holes, and voids of various dimensions of a space; it keeps track of cavities of various dimensions via homology classes, each of which has a representative 'cycle'. Cycles are $d$-dimensional loops surrounded by cliques. For any simplicial complex, we can compute its homology classes for each dimension.

**Weighted Rank Clique Filtration.** In this study, the nodes are AAL2 brain regions, and we derive simplicial complexes from the symmetric connectivity matrix (see Section 2.2.2)

using a process called the Weighted Rank Clique Filtration (WRCF). A "filtration" refers to a process of creating a sequence of increasingly detailed simplicial complexes, each containing its predecessor, where the starting simplicial complex consists of $N$ disconnected nodes. For the WRCF, at each step, the next connection from the ordered connectivity matrix is added. After a maximum of $\binom{N}{2}$ steps, we obtain a fully connected $(N-1)$-clique. For our filtrations, the ordering always starts with the strongest connection unless we specify the 'reverse filtration'.

Homology groups can be computed for each simplicial complex in the filtration. The inclusion maps between successive simplicial complexes induce maps between these homology groups, resulting in a notion of a 'persistent homology group' [Zomorodian and Carlsson, 2005] which tracks homology classes that remain non-trivial across the filtration. Cavities corresponding to homology classes and persistent homology classes can be specified by a representative 'cycle'. PH makes it possible to track the evolution of topological cavities through the filtration

Figure 2 shows a toy example of an ordered $10 \times 10$ symmetric matrix together with a visualisation of the evolution of the simplicial complexes throughout the filtration. The filtration starts with 10 disconnected nodes; the strongest connection is between nodes $A$ and $B$ (indicated by '1' in the matrix of integers), the second strongest is between nodes $C$ and $D$ (indicated by '2'), etc. As the filtration progresses and connections are added step-by-step, structure in the form of 'cycles' emerges and vanishes. For example, 1-cycles are formed (or are 'born') in steps 4 and 8, with constituent nodes, ABCD and GHIJ, respectively. In step 16, a 2-cycle is formed (constituent nodes ABCDEF), and in step 12, the 1-cycle, ABCD, 'dies' because it is now the boundary of a linear combination of 2-cliques.

There are as many steps of the filtration as there are unique values in the ordered matrix $O$, so a maximum of $\frac{N(N-1)}{2}$ for an $N \times N$-matrix. For the matrices obtained from the data, the filtration steps were normalised by dividing by the total number of filtration steps, resulting in filtration steps indexed by (rational) numbers in the range $[0, 1]$, enabling comparison between filtration of different length.

**Persistence barcodes and persistence landscapes** Given a cycle indexed $i$ with birth time $b_i$ and death time $d_i$ in terms of (normalised) filtration steps, we can associate it to an interval called a 'barcode', $(b_i,\ d_i)$. Hence, for each topological structure (cycle) uncovered using persistent homology, we have its associated barcode, and the results can be summarised in a multiset of $P$ persistence barcodes $\{(b_i,\ d_i)_{i=1}^{P}\}$. We shall segregate the barcodes by dimensionality of cycle.

It is helpful to further convert barcodes into persistence landscapes [Bubenik and Dłotko, 2017]. This information-preserving transformation enables statistical analyses, which are not possible with a discrete multiset of barcodes. For a barcode with birth time $b$ and death time $d$, $(b, d)$ with $b < d$, a piecewise linear function $f_{(b,d)} : \mathbb{R} \to [0, M]$ is defined as:

$$f_{(b,d)}(x) = \begin{cases} 0 & \text{if } x \notin (b, d) \\ x - b & \text{if } x \in (b, \frac{b+d}{2}) \\ -x + d & \text{if } x \in (\frac{b+d}{2}, d) \end{cases} \tag{2}$$

where M is a real number representing the end of the filtration, e.g. number of filtration steps. In this study, we have normalised this to 1. It is now possible to construct a persistence landscape for a multiset of barcodes $\{(b_i, d_i),\ i = 1, \ldots, P\}$, as a set of functions $\lambda_k : \mathbb{R} \to \mathbb{R}$ defined pointwise, such that for each $x$, $\lambda_k(x)$ is the $k$-th largest value of $\{f_{(b_i,d_i)}(x)\}_{i=1}^{P}$ and $\lambda_k(x) = 0$ when there is no $k$-th largest value (the index $k$ denotes the layer of the landscape).

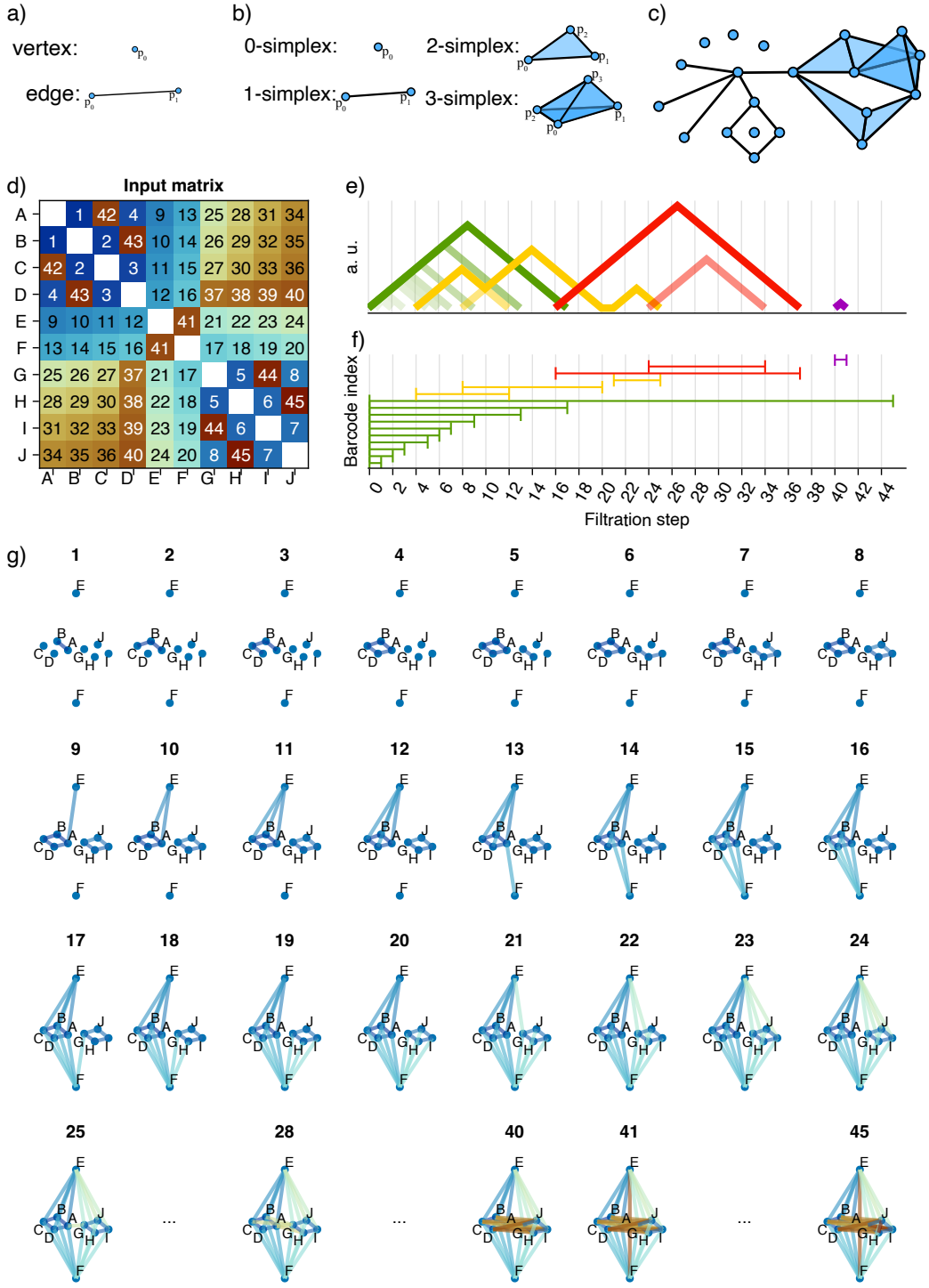


Figure 2: (a) Building blocks of a graph. (b) Building blocks of a simplicial complex. (c) Simplicial complex. (d) A toy example of weighted-rank clique filtration derived from an ordered matrix. The results for dimensions $d = 0, 1, 2, 3, 4$ are colour-coded in (e) and (f) as green, yellow, red, blue, purple, respectively. (d) An example of the ordered matrix; colours correspond to the filtration step; (e) persistence landscapes derived from the filtration; (f) barcodes derived from the filtration (g) simplicial complexes created at the filtration step are annotated above the figures; some steps are omitted, i.e. after all cycles died in dimension 1 (step 25) and before a fully connected graph is formed (step 45), with a few exception, e.g. when a cycle in dimension 4 is formed and dies (steps 40 and 41 respectively). The horizontal axis for (e) and (f) are filtration steps, and there are as many filtration steps, as there are unique numbers in the ordered matrix.

Unlike a multiset of barcodes, a collection of persistent landscapes can be averaged; the averaging operation is performed layer by layer on the functions $\lambda_k$ for each $k$ to obtain an

averaged persistence landscape, see Supplementary Figure Supp.A.2 for an example. This allows for statistical analysis of the differences in the persistence properties between various groups.

To give some intuition about the relation between the connectivity structure and topological properties (cycles, birth times, and persistence), we present three toy examples in Figure 3. Here, all three $8 \times 8$ connectivity matrices possess a 1-dimensional cycle (ABCD) with the same structure connecting the same four nodes. In (a) and (c), this cycle is born early when very few (only 4) connections have been added to the clique complex. In (b), it is born later, when there are already 15 connections in the clique complex before the formation of the cycle. The cycle, however, is more persistent in (c) because it is only 'killed' at step 25 of the filtration and therefore has a lifetime of 15 steps. The same cycle derived from matrices in (a) and (b) has, in both cases, a lifetime of only 10 filtration steps.

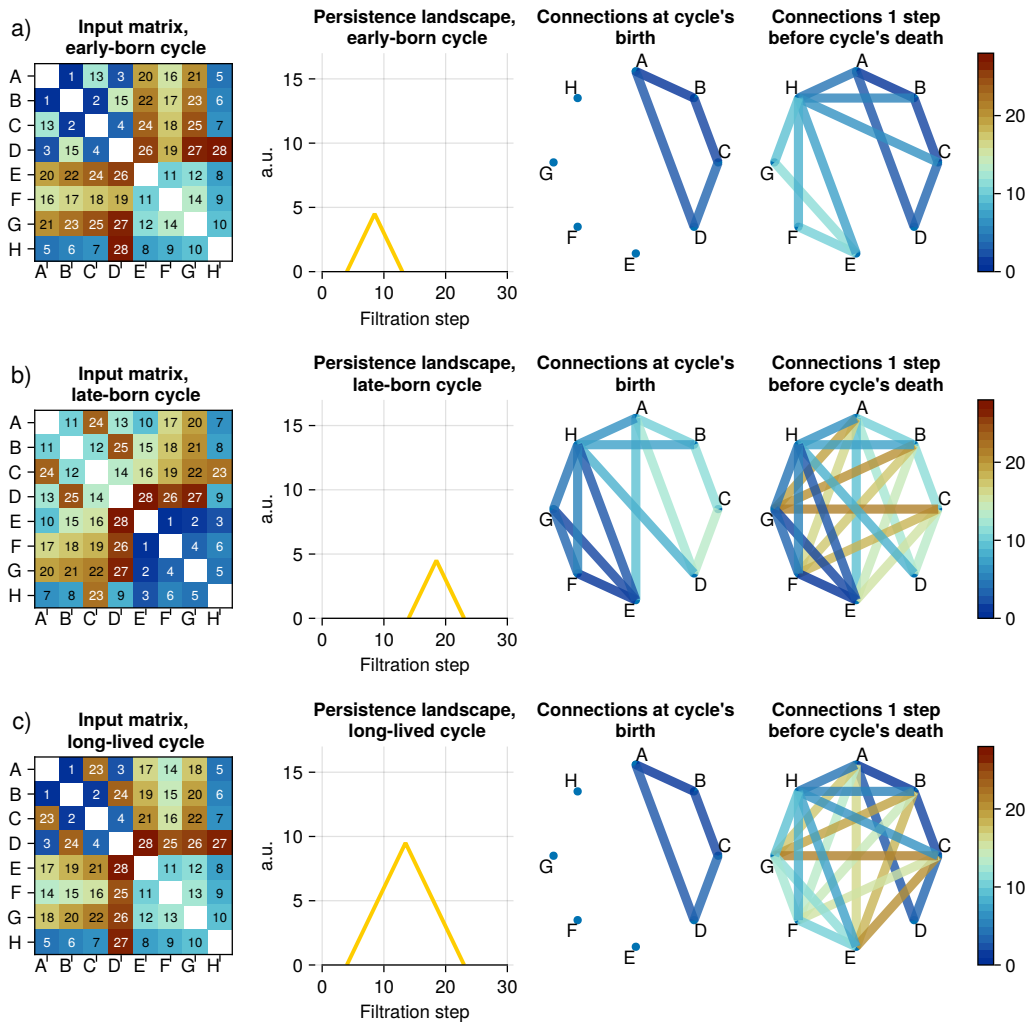


Figure 3: Toy examples illustrating differences in persistent sublandscapes given different birth time and persistence of a cycle that is present in all three cases. Each row presents an example of a topological structure, with a) an early-born and short-lived cycle (top row); b) a late-born and short-lived cycles (middle row); c) early-born and long-lived cycle (bottom row). Figures in columns are (from left to right): input ordered matrix, related persistent landscape in dimension 1, visualisation of the nodes' connectivity when a cycle is born and 1 step before it dies (the colour bar corresponds to numbers in the ordered matrix). In each of the structures, only one cycle was created in the filtration process.

If these matrices represented connectivity structures in the brain from three different people, it would show that although each person possessed exactly the same connectivity pattern (or 'cycle'), in other words, a physically indistinguishable set of white matter tracts between the specific nodes comprising the cycle, the strength of this pattern relative to the rest of the person's connectome was, nevertheless, very different. The extent of this difference

can be seen and quantified by the very different persistent sublandscapes associated to the cycle for each person.

Differences in landscape structure were investigated using permutation tests on landscape distances [Bubenik, 2015]. The test statistic is the $L_1$-distances between two averaged landscapes for each dimension $d$ compared to the distribution of $L_1$-distances obtained from randomized landscapes. The details of this procedure are presented in Supplementary Methods Section A.2.4.

## 2.4 Null models

We compared the topological descriptors derived from the data with four types of null models: The 'Frankenstein-brain', the "Euclidean brain", the "Geometric" null model and the Random null model.

For all models ('Frankenstein-brain' NM, 'Euclidean-brain' NM, Geometric NM, and Random NM), the matrices were of the same size as the connectivity matrices computed from the data ($94 \times 94$).

**'Frankenstein-brain' null model (random weight permutation)** This null model (NM) utilizes (*COBRE*)population data by altering connectivity matrices through random weight swaps. That is, in a null connectivity matrix of a (simulated) subject, every edge was replaced with a probability $p$ with a connection between the same regions, but from a randomly selected participant from within the group, with the selection being made such that all other subjects have the same chance of being chosen. We generated 6 populations of 88 matrices for a range of probabilities $p = \{0.05, 0.1, 0.2, 0.5, 0.9, 0.99\}$. The matrices created for the data-based null model were generated and organised into two groups, one from each group of subjects in the *COBRE* dataset. Swapping connections between subjects removes individual contribution while preserving the global relation between brain regions (if there is any).

**'Euclidean-brain' null model** This NM was constructed based on the concept of a minimally wired brain network [Betzel and Bassett, 2017, Sizemore et al., 2018]. In this model, the connectivity is given by the Euclidean distance between the brain regions of the used atlas. Firstly, 94 brain regions from the AAL2 atlas were represented as nodes, with their spatial positions defined by three-dimensional coordinates given by the centre of the brain region in MNI space [Evans et al., 1992, Brett et al., 2002] (a standardised coordinate system used to locate brain structures created by the *Montreal Neurological Institute*). The coordinates of the regions from the MNI brain were normalised to lie within the unit cube $[0, 1]^3$ for consistency. Secondly, 6 populations, each consisting of 88 spatial distribution matrices, were generated by adding Gaussian noise to the coordinates to introduce variability, each population with mean $\mu = 0$ but different standard deviation levels, $\sigma = \{0.0005, 0.005, 0.01, 0.02, 0.05, 0.1\}$. Finally, connectivity matrices were constructed with the weight determined by the inverse of the Euclidean distance between the paired nodes: $w_{i,j} = \frac{1}{d(i,j)}$, where $d(i, j)$ is the Euclidean distance between nodes $i$ and $j$. This approach emphasises connections between spatially proximal regions, embodying the minimally wired aspect of the network and reflecting spatial constraints in brain wiring. The visualisation of node distribution is presented in the Supplementary Figure Supp.B.30.

**Geometric null model** This NM, also used in [Giusti et al., 2015b], is where $N \times N$ connectivity matrices $M^{geom}$ consist of pairwise Euclidean distances between a set of $N$ points uniformly distributed in a unit cube in $\mathbb{R}^d$.

**Random null model** In the Random NM, a connectivity matrix $M^{rand}$ is a symmetric order matrix where (without loss of generality) the upper diagonal entries have been permuted randomly.

# 3 Results

An overview of the data preprocessing pipeline and topological analysis is provided in Supplementary Figure Supp.A.1.

We found that many persistent homology class representative cycles are found in multiple subjects in both the schizophrenia (SCH) and healthy (HC) groups. However, a subset of shared cycles exhibited significant differences in their persistence properties between groups.

## 3.1 Cycles derived from the *COBRE* data

Full results are shown in Figure 4 (dimensions 0 and 1), and Supplementary Figure Supp.B.3 (dimensions 2 and 3). Each column in these figures represents a distinct cycle, with part (v) showing its persistent barcodes (one from each person possessing the cycle). Transparency in the barcode plots reflects the number of subjects sharing a cycle at similar filtration levels—darker regions indicate greater overlap. Part (ii) displays binary vectors indicating which AAL2 atlas nodes are involved in each cycle, arranged via agglomerative clustering, which is performed separately for each dimension (see Supplementary Section A.3 for details). The corresponding dendrograms are shown in part (i).

Intriguingly, this independent agglomerative clustering on the anatomical nodes automatically gave rise to clusterings of persistent bar codes (shown in parts (v)), indicating that anatomically similar cycle classes often possess bar codes with similar birth and death times. This is particularly striking because the hierarchical clustering only uses the vectors of brain areas and Hamming distances and is blind to the topological analysis (persistence information).

In dimension $D = 0$, cycles are connected components present in the connectome at various scales. They are all born at time 0 and gradually merge with each other. It can be seen in Figure 4a that all such cycles have merged into a single component 16% of the way through the filtration, as all cycles (except the one that survives forever) die by 0.16. For dimensions $D = \{1, 2, 3\}$, cycles share multiple brain regions as shown in Figure 4b($ii$) and Supplementary Figure Supp.B.3($ii$).

Cycle popularity, defined as the number of subjects in which a cycle appears, is visualized in the raster plots of parts (ii). There are cycles in dimensions 0 and 1 that were repeatedly found in multiple subjects. However, shared cycles were the minority compared to the unique cycles that were found in only single subjects ("singletons"). In dimension 1, out of 1625 distinct cycles, 1130 cycles (69.53%) were singletons. A similar observation can be made for cycles in dimension 0.

Structures for dimensions 2 and 3 are more individualised and very few are shared as most of the cycles are singletons, but their structure as shown in Figure Supp.B.3($ii$) is, to a large extent, similar to some dimension 1 popular cycles, as they are often formed when dimension 1 cycles are killed. Two and three-dimensional cycles are also constructed out of more nodes than lower-dimensional cycles (total nodes per cycle, for dimension $D$: $1.97 \pm 0.17$ ($D = 0$), $10.44 \pm 5.24$ ($D = 1$), $15.61 \pm 8.58$ ($D = 2$), $12.93 \pm 3.76$ ($D = 3$)). We observe that we can cluster these high-dimensional cycles into larger chunks as presented in Supplementary Figure Supp.B.4. We observe many 'variant' cycles in clusters with slight variations between individuals but with considerable overlap; this is analogous to the fMRI finding in [Gordon et al., 2017] which showed that spatially variable 'network variants' appear to exist for all individuals and differed in small ways from those obtained from group-averaged data analyses, e.g. [Yeo et al., 2011].

Despite their uniqueness, many singleton cycles in dimension 1 were structurally similar to popular cycles. Due to the non-uniqueness of the cycle representation, these could nevertheless stem from the same underlying persistent homology class. This was not observed in the Random or Geometric null models, e.g. Supplementary Figure Supp.B.25 shows that for the connectivity matrix arising from the distance matrix derived from randomly chosen points in the unit cube in $\mathbb{R}^5$ (other dimensions yield analogous results), the clustering of the node structures of representative cycles did not yield coherent patterns in structure, popularity, or persistence.

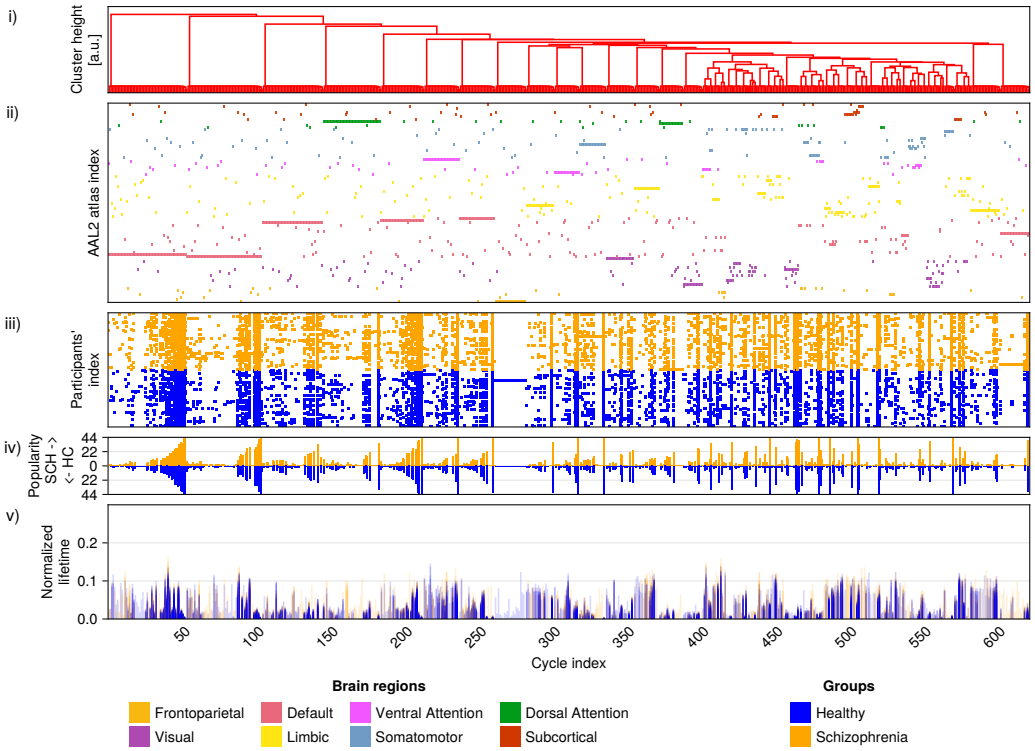


(a) Dimension 0

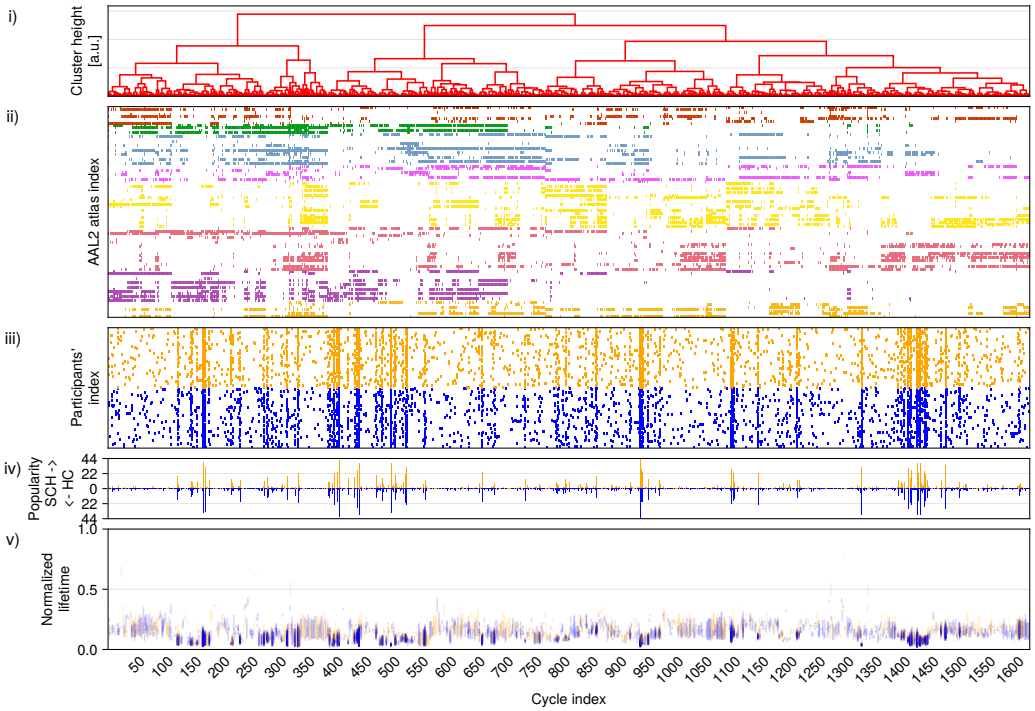


(b) Dimension 1

Figure 4: Exploration of structure, popularity and topological properties of unique cycles in dimensions 0 and 1. Raster plots in (ii) are showing which brain regions participated in the unique cycles at the moment of the cycle's birth (more details about the structure of selection of cycles are presented in the Supplementary Results Section B.11). All unique cycles are aligned with the horizontal axis and brain regions are marked with 7 colours according to their Yeo's [Yeo et al., 2011] functional network atlas. The brain regions are ordered according hierarchical clustering; the corresponding dendrogram is shown in (i). Raster plots in (iii) are showing in which subjects, a cycle was found (orange used for SCH, blue for HC). Plot in (iv) summarises the individual cycle's popularity, i.e., the total number of subjects per group, in which a cycle was found. In (v), the (vertical) persistence barcodes for each cycle. The vertical axis shows the lifetime normalised to the maximal filtration step in the filtration. All horizontal axes within (a) and within (b) are the same, using cycle indexing from hierarchical clustering.

## 3.2 Persistence landscapes.

We examine differences in the persistence landscapes between the SCH and HC groups of the *COBRE* dataset, firstly looking at global landscapes, followed by a more fine-grained study of sublandscapes.

### 3.2.1 Global persistence landscapes.

Figure 5 shows the averaged global landscapes computed for the two studied groups: $Y^D_{SCH}$ and $Y^D_{HC}$, for dimensions $D = 0, 1, 2, 3$, as well as the layer-by-layer differences '$Y^D_{HC} - Y^D_{SCH}$' between these landscapes.

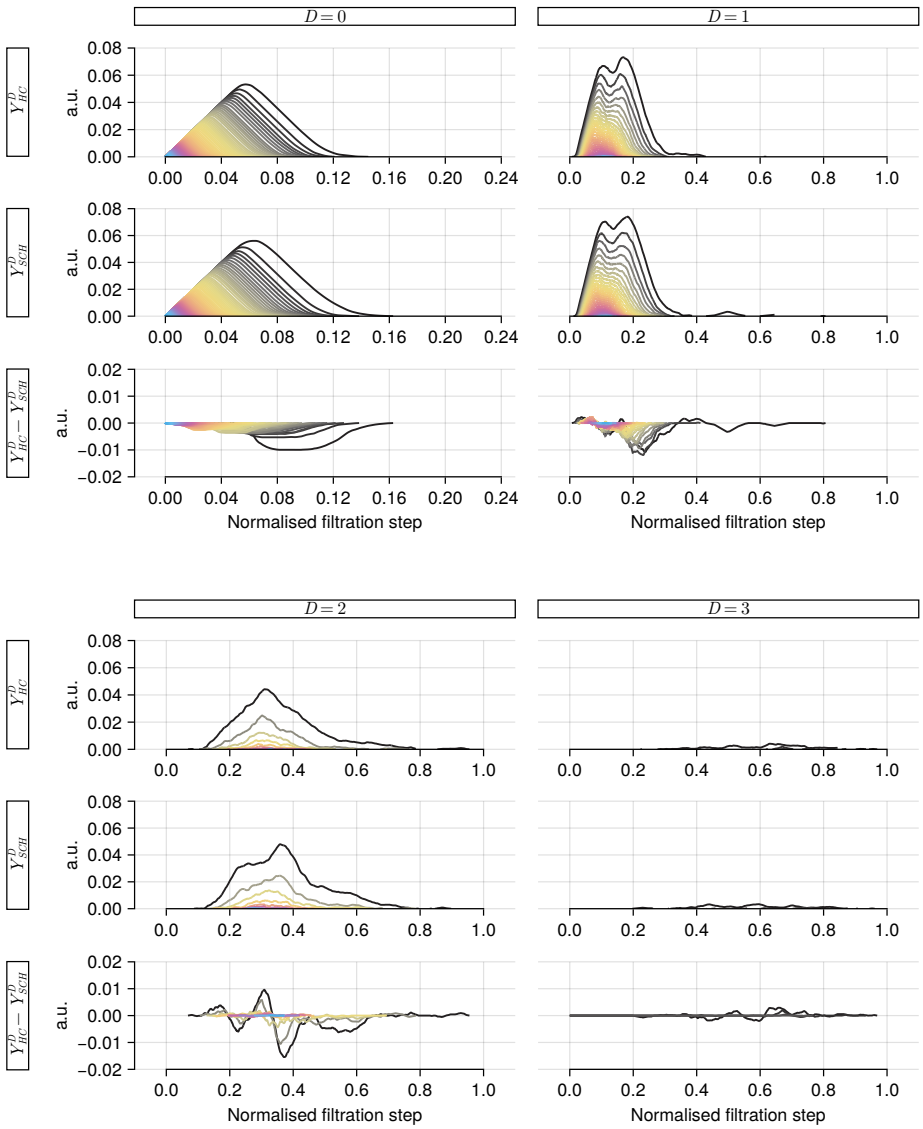


Figure 5: Average global persistence landscapes for healthy controls $Y^D_{HC}$, schizophrenia subjects $Y^D_{SCH}$ and the difference $Y^D_{HC} - Y^D_{SCH}$ for topological features in dimensions $D = 0, 1, 2, 3$, as indicated by subtitles and labels on the left-hand side. The horizontal axis represents the filtration step normalised to the total number of steps in each filtration (the range for dimension 0 is limited to filtration value 0.24, the full range shown for other dimensions). The vertical axis is the height of the landscape expressed in arbitrary units ($Y^D_{HC}$ and $Y^D_{SCH}$ are shown in the same scale). The colours in the persistence landscapes are related to the landscape layer- the outer layers (e.g. $\lambda_0$) are denoted with black, then the colour scheme goes from yellow to pink and then to blue for deeper layers.

We observed significant differences in the global persistence landscapes between schizophrenia *SCH* and healthy control *HC* groups in dimensions 0 and 1. Specifically the landscapes

for $SCH$ subjects denoted, $Y^0_{SCH}$ and $Y^1_{SCH}$, were significantly more persistent than those for $HC$ subjects, $Y^0_{HC}$ and $Y^1_{HC}$, as determined by a one-sided permutation ($n = 10000$) test as described in Supplementary Section A.2.4 (dimension 0: $p = 0.014$; and dimension 1: $p = 0.018$). These differences are visualised in Figure 5, where layer-by-layer differences $Y^D_{HC} - Y^D_{SCH}$ (for $D = \{0, 1\}$) are predominantly negative, indicating greater persistence in the $SCH$ group across all layers.

For dimension 1, all cycles are born in the early stages of filtration (average birth time $0.088 \pm 0.058$), therefore they are formed with strong connections. While a cycle is created (born) with strongly connected brain regions (we will call brain regions participating in the cycle at birth, a frame), at the same time, the cycle has to be "empty"- none of the combinations of brain regions within the frame are strongly connected. Thus, the cycles are twofold important- they indicate between which brain regions there are strong connections, but at the same time, cycles represent the state of connectivity as a whole, showing which connections are not present (at the moment of cycle formation).

No statistically significant differences were found in the average global persistence landscapes for dimensions 2 and 3 (one-sided permutation test, $p = 0.205$; and $p = 0.509$ respectively),

### 3.2.2 Sublandscape analysis identifies candidate biomarkers

For each cycle found in at least 25% of the participants ('popular cycles'), we performed permutation tests (Section A.2.4) on the associated sublandscapes to examine group differences in their persistence, controlling for multiple comparisons using the Benjamini-Hochberg (BH) procedure for False Discovery Rate (FDR). Among the significantly different cycles, three were found in at least 44 subjects (50% of the subjects) and showed significant group differences, suggesting their potential as candidate biomarkers for schizophrenia.

**Popular cycles for dimension 1.** Out of a total of 55 popular dimension 1 cycles, 22 cycles are significantly different (5 more cycles with p-values below 0.05 did not survive the FDR correction). A complete set of popular sublandscapes and sublandscape distance distributions under the permutation test can be found in Supplementary Section B.5 in Figures Supp.B.8 -Supp.B.12. The group-averaged sublandscapes corresponding to each popular cycle individually are shown in Supplementary Figure Supp.B.5.

**Sub-landscape centroids reveal distinct patterns of disruption** Centroids (Section A.3) were used to characterise qualitative differences between the sublandscapes of the two groups (see Figure 6-a). Vectors were drawn from the $HC$ centroid to the $SCH$ centroid for each cycle and plotted in polar coordinates in Figure 6-b. Agglomerative clustering of these vectors based on cosine distance (Figure 6-c) confirms two distinct clusters reflecting two types of changes in brain organisation seen in schizophrenia.

The first cluster in red (cycles 26, 40, 46, 52) comprises persistence sublandscapes that are all 'lower' for $SCH$ than in $HC$ due to earlier death times for $SCH$ cycles. The second cluster in green (18 cycles) comprises of persistence sublandscapes that are mostly shifted upwards and right for $SCH$ compared to $HC$. Consult Supplementary Section B.3 for a more detailed discussion on sublandscape differences. Structures found in schizophrenia-affected patients are therefore "delayed" (both are dying later, while some are also born later). The shift is consistent with the fact that inner layers of the dimension 1 global landscape, to which sublandscapes contribute, are formed later for SCH than for HC due to weaker connections (both birth and death of cycles for SCH are occurring later in the filtration). This agrees with the structural evidence for the disconnection of brain regions in schizophrenia [Ellison-Wright and Bullmore, 2009, Kelly et al., 2018].

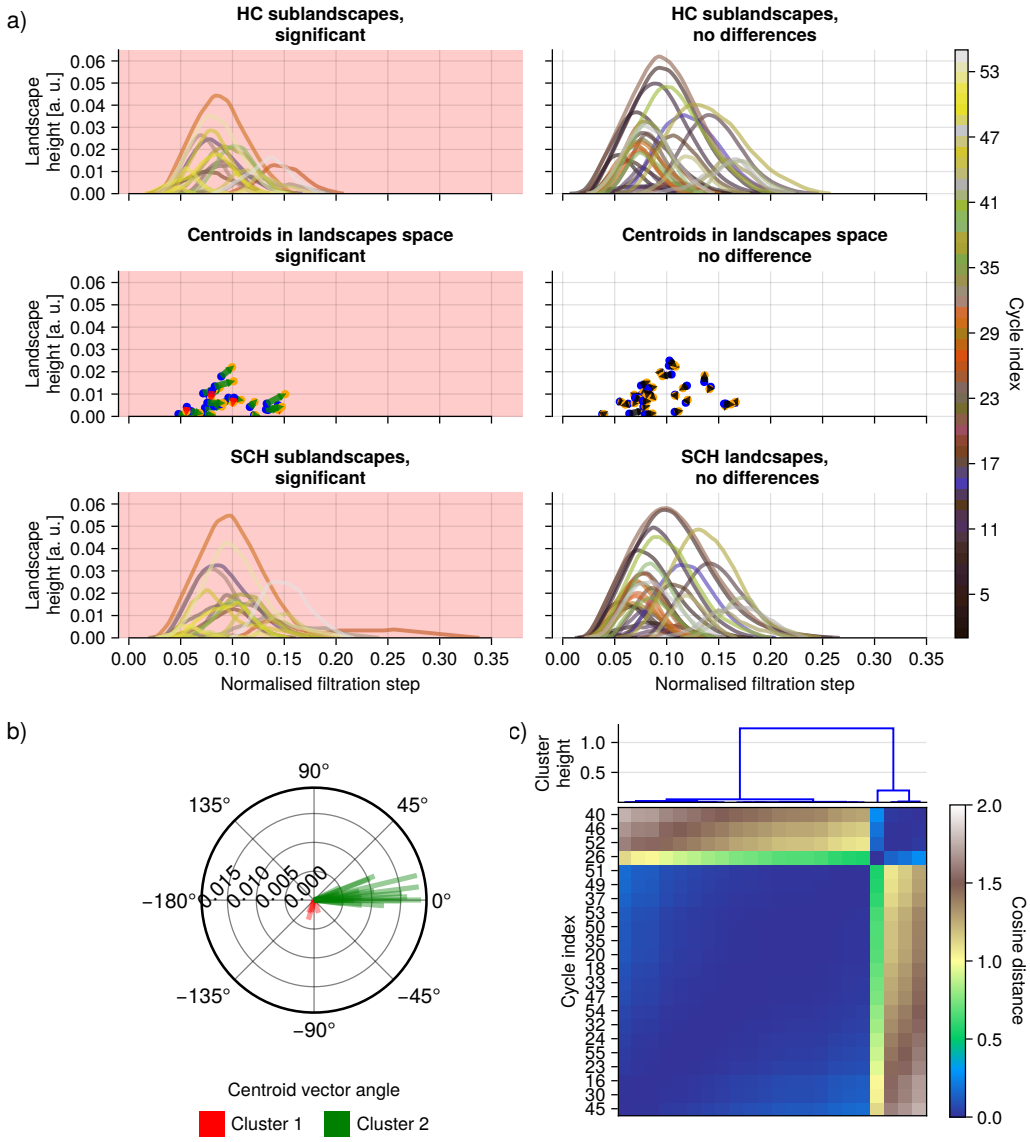


Figure 6: Decomposition of the global landscape in terms of popular sublandscapes (a) (data for cycles in dimension 1), the polar plot of centroid difference vectors (b) and cosine distance matrix with clustering (c). In the middle plot of (a), each arrow indicates how the centroids in dimension 1 are displaced for the 22 popular persistence sublandscapes that were found to be significantly different between the two groups (popular cycles were cycles found in at least 22 subjects). In the top and bottom rows of (a), persistence sublandscapes are presented for the HC group (top) and the SCH group (bottom), for statistically different cycles (first column) and for cycles where no significant difference was found (second column). Persistence sublandscapes are coloured according to the cycle they are derived from, i.e. the same colour in HC and SCH is used for the same cycle. The vectors shown in (b) indicate the direction of the centroids shift in the cycles in dimension 1 that are significantly different between *HC* and *SCH* group. Clustering (c) indicates two distinct groups, cluster 1 (cycles 26, 40, 52, 56) marked as red, cluster 2 with the remaining cycles. Vectors in the raster plot indicate how the centroid of *SCH* is placed when compared to equivalent cycle in the *HC* group.

### 3.2.3 Dimension 1 cycle structures and brain regions.

We note that many of the brain regions partaking in the significant dimension 1-cycles are frequently mentioned in existing literature about structural brain alterations induced by schizophrenia. In general, cycles differ in both their size (total number of brain regions participating in a cycle) and in the regions involved. However, some regions are repeatedly found in many of the significant cycles - 9 brain regions were found in at least 4 cycles. We summarise these in Table 3; for further discussion on the connections to existing literature, see Supplementary Results Section B.4. A full list of cycles and their constituent regions can be found in Supplementary Table B.11.

Table 3: Areas that partake in significant Dimension 1 cycles and the schizophrenia literature

| AAL2 Area | Cycles it occurs in | Literature |
|---|---|---|
| 71. *Left precuneus* | 16, 18, 23, 30, 33, 40, 52, 54 | [Ottet et al., 2013], [Sambataro et al., 2010], [Zhao et al., 2018] |
| 49. *Left cuneus* | 18, 23, 33, 50, 52, 54 | - |
| 63. *Left superior parietal gyrus* | 30, 33, 40, 51, 52, 54 | [Howes et al., 2023], [Ottet et al., 2013], [Wheeler and Voineskos, 2014] |
| 65. *Left inferior parietal gyrus* | 30, 33, 40, 51, 52, 54 | [Merritt et al., 2021], [Wheeler and Voineskos, 2014], [Vita et al., 2012] |
| 72. *Right precuneus* | 16, 18, 23, 24, 49 | [Cropley et al., 2017], [Shen et al., 2023] |
| 50. *Right cuneus* | 18, 23, 49, 50 | - |
| 38. *Right middle cingulate & paracingulate gyri* | 16, 24, 30, 46 | [Howes et al., 2023], [Li et al., 2015] |
| 56. *Left middle occipital gyrus* | 33, 51, 52, 54 | [Canu et al., 2015] , [Cropley et al., 2017], [Howes et al., 2023], [Osimo et al., 2019], [Witthaus et al., 2008], [Zhao et al., 2018] |
| 60. *Right fusiform gyrus* | 26, 32, 37, 47 | [Howes et al., 2023], |

**Significant cycles with low persistence** Persistence landscapes 20, 35 and 53 are constructed from small cycles (4 brain regions involved in each) with very low persistence and show significant variability in their landscapes. Cycles with low persistence are typically considered to be noise in TDA. However the fact that they were found across multiple subjects (in 44, 32 and 23 subjects, respectively), and at least two regions for each one of the cycles are reported in the literature to be affected by schizophrenia (see Supplementary Table 5), suggest that they are not noise-related structures, but potentially important features. The significance of low-persistence cycles has already been reported in the applications of TDA to medical data [Kanari et al., 2018,Bendich et al., 2016], in particular, in a study of connectivity in functional magnetic resonance imaging [Stolz et al., 2017].

### 3.2.4 Cycle Laterality

We examined the hemispheric distribution of the 55 popular dimension-1 cycles to assess structural asymmetry. Table 4 summarises which significant cycles were lateralised (left- or right-hemisphere), symmetric, or could not be classified. Among popular cycles, we observed a strong asymmetry: 16 cycles were confined to a single hemisphere, and none of these had a corresponding "mirror pair" composed of anatomically equivalent regions in the opposite hemisphere within popular cycles, as defined by the AAL2 atlas (see Supplementary Results B.2.2).

Among the full set of popular cycles, we identified eight "mirror twin" pairs—cycles composed of homologous regions in opposite hemispheres. Of these, three pairs included one significantly different cycle (cycles 26, 37, and 47—all right-lateralized) and one non-significant counterpart (cycles 42, 48, and 34, respectively). The remaining five pairs were composed of non-significant cycles. A visualization can be seen in the frequency scaffolds in Supplementary Figure Supp.B.7.

Hemispheric asymmetry in healthy brain structure has been widely observed [Toga and Thompson, 2003,Hervé et al., 2013] in both grey [Good et al., 2001,Watkins et al., 2001,Lancaster et al., 2003] and white matter [Cao et al., 2003,Takao et al., 2011a,Takao et al., 2011b]. In schizophrenia, deviations from typical lateralization patterns have been reported, e.g. as mean diffusivity lateralisation abnormalities (among others, reduction in left *superior longitudinal fasiculus* ) [Ho et al., 2017] or reduced hemispheric asymmetry of global integration in patients compared with healthy controls in the study by Sun et al. (2017) [Sun et al., 2017]. Specifically, the last study reports a significant reduction in nodal efficiency in schizophrenia patients in *fusiform gyrus*, *parahippocampal gyrus*, *superior temporal gyrus*, *inferior temporal gyrus*, *inferior parietal lobule* - it is notable that all but the last are regions found in the

lateralised significant cycles 26 and 47.

Table 4: Laterality of significant dimension 1 cycles

| Laterality | Cycles exhibiting property |
|---|---|
| Left | 20, 33, 40, 51, 52, 53, 54, 55 |
| Right | 24, 26, 32, 35, 37, 45, 47, 49 |
| Symmetric | 16, 18, 23, 50 |
| Mixed | 30, 46 |

## 3.3 Null models

Since the brain is far from having a random structure [Bullmore and Sporns, 2012, Sporns, 2013], we expected that there should be structures that are repeated among subjects. At the same time, we also expect to see individual variability and therefore structures that are observed in only subsets of subjects. Null models (NM) (see Section 2.4 for descriptions) were used to explore the underlying structure of the data and to give possible causes for the similarities and variability found. Full details of this analysis can be found in Supplementary Results Section B.8.

## 3.4 Cross-Dataset Structural Consistency

Despite differences in acquisition protocols between the *COBRE* and *HCP* datasets (see Table 2), we observed a high degree of structural overlap. All 55 popular cycles identified in *COBRE* were also present in *HCP*, indicating strong cross-dataset reproducibility. This is visually evident in Figure 7(*iii*), where vertical lines representing frequently observed cycles in HC (blue) and SCH (orange) subjects from *COBRE* also appear in *HCP* subjects (red). For full sublandscape results, see Supplementary Section B.6.

In dimension $D = 1$, 64 cycles showed significantly different popularity between *COBRE* and *HCP*. Of these, 13 cycles also exhibited significant differences in persistence sublandscapes between SCH and HC groups (cycles 16, 20, 23, 24, 26, 30, 37, 45, 47, 49, 51, 54, 55). An additional 9 cycles (18, 32, 33, 35, 40, 43, 50, 52, 53) showed significant differences in sublandscapes between SCH and HC but did not differ in popularity across datasets. For full results of popularity significance tests, see Supplementary Results Section B.7.

Popular cycles also showed low variability in their birth time compared to non-popular cycles (Mann-Whitney U test on the distribution of standard deviation of birth times of cycles found in more than 22 subjects vs standard deviation of birth times of cycles found in more than 3 but less than 22 subjects, $U_{COBRE} = 5666.0$, $p_{COBRE} = 0.009$, $U_{HCP} = 4180.0$, $p_{HCP} = 0.0005$). This suggests that such cycles represent stable features of brain architecture.

The fact that common cycles are found across datasets allows for comparisons of connectomes across datasets recorded using different scanners.

### 3.4.1 Reverse filtration

The weakest connections in the connectivity matrix may be indicative of measurement noise and not actual connections [Fornito et al., 2016]. Therefore, we expect that the numbers of cycles that emerge from reversing the filtration (starting from the weakest) would be similar to that coming from various random null models.

Figure 8, shows Betti curves (see equation A.3 for a definition) from the data matrices and NMs for both forward and reverse filtrations in dimensions $D = [0, 4], D \in \mathbb{Z}$, Due to the sparsity of the connectivity matrices for the *COBRE* data (which have on average $2238.68 \pm 501.78$ zero entries), in the reverse filtration of *COBRE*, $\beta_0$ starts off low as there are very few connected components (and not 94 - one for each detached node, as is the case for other models). On the other hand, the *COBRE* $\beta_1$ curve starts with a few cycle representatives, whereas all others start with no dimension 1 cycle representatives.

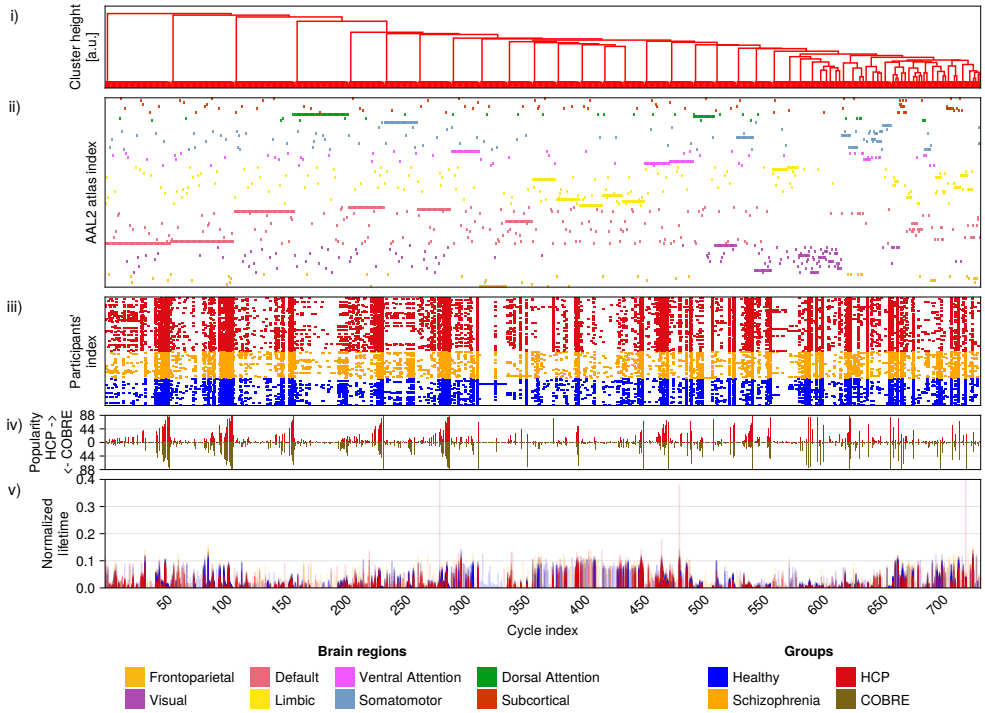


(a) Dimension 0

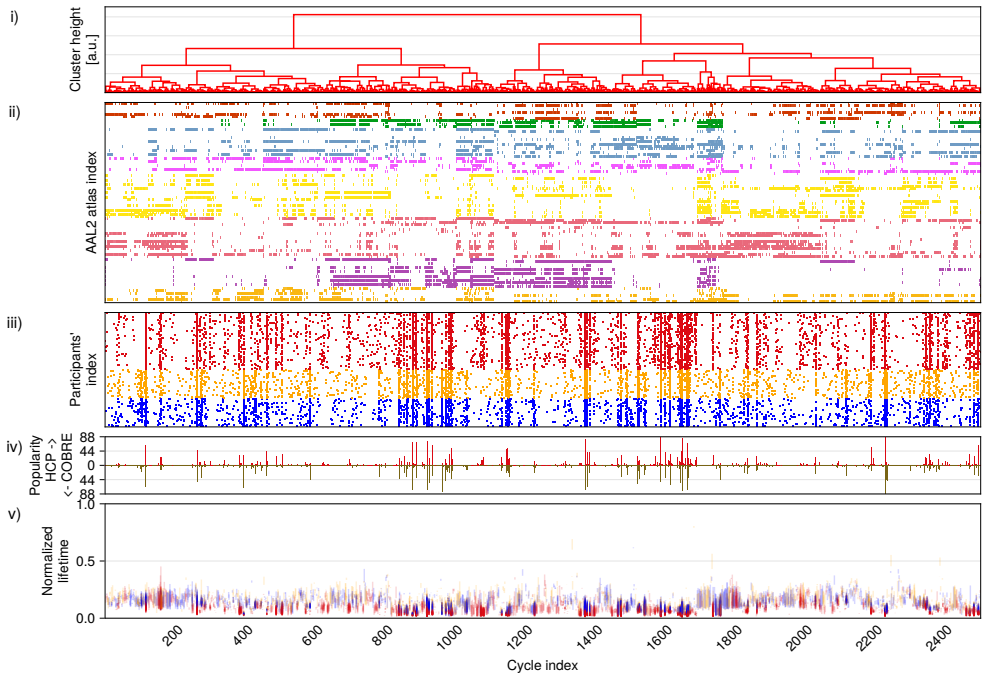


(b) Dimension 1

Figure 7: Unique cycle structures and popularity presented as a raster plot for dimensions $D = 0, 1$ for Human Connectome Project (*HCP*) and *COBRE*. For each figure, the plots are structured as described in 4. Plots (ii) are raster plots showing which brain regions participated in the unique cycles at the moment of the cycle's birth. All unique cycles are aligned with the horizontal axis and brain regions are marked with 7 colours according to Yeo's functional network atlas. The brain regions are ordered according to the hierarchical clustering presented at the top part of the plot. Plots (iii) are raster plots showing in which subjects a cycle was found (orange is used for SCH, blue for HC). Plot (iv) summarizes individual cycle popularity, i.e. total number of subjects, in which a cycle was found. (v) Vertical persistence barcodes for each cycle. The vertical axis shows the lifetime normalised to the maximal filtration step in the filtration. All horizontal axes are the same, using cycle indexing from hierarchical clustering.

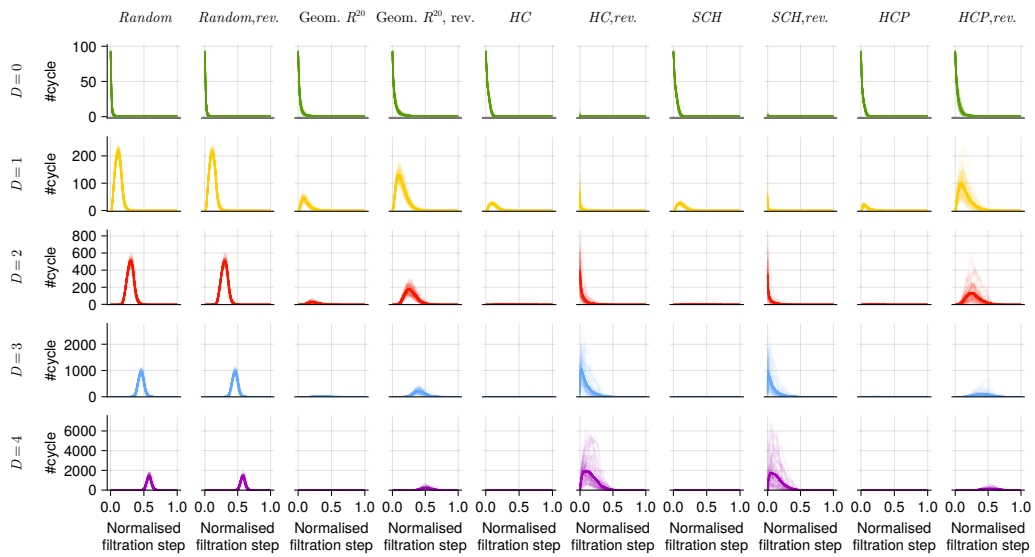


Figure 8: Comparison of Betti curves for Random NM, Geometric $R^{20}$ NM, *COBRE*, *HCP* and their reverse filtration for dimension in range $0 \leq D \leq 4, D \in \mathbb{Z}$ for matrix size $94 \times 94$. Solid curve shows the average Betti curve computed from 44 samples; each individual sample is shown with a faint line.

The distribution of Betti curves for the reverse filtration for *COBRE* resembles the distribution of Random NM in that they exhibit unimodal Betti curves with peak values that increase with dimension, $D$, unlike e.g. Geometric NM Betti curves where peaks decrease with increasing $D$ for $D \geq 1$, as shown in [Kahle, 2013, Giusti et al., 2015b]. Interestingly, it has more cycles in dimensions $D = 3, 4$ than for Random NM, some of which stem from the large number of zeros present in the original matrix, which leads to large structures at the very beginning of the filtration. Matrices where the Betti curves are higher than those for random matrices have not been reported on or systematically studied as far as the authors are aware; so the connectivity of white matter has interesting mathematical properties. For the *HCP* dataset, however, the distribution of Betti curves for the reverse filtration resembles that for Geometric NM. In Supplementary Figure Supp.B.22 we present results for $D = 0, \ldots, 8$, for submatrices of size $30 \times 30$ from both datasets, obtained by taking only the first 30 AAL2 brain regions. Limiting the matrix size in this way allowed sufficient computational resources for investigating higher-dimensional structures. Here, the distribution of Betti curves for both datasets follows the distribution of the Random NM.

There are always more unique cycles for the data (details are presented in Supplementary Table 9) as compared to null models, especially in the forward filtration. This is particularly visually evident in Supplementary Figures Supp.B.25, Supp.B.27 for the randomised models.

**Shuffling weak connections** In the Supplementary Section B.9.1, we show how shuffling the $k \in \{10, 20, 30, 40, 50, 60, 80, 90\}$ per cent of the weakest connections in a selected matrix from *HCP* affects the Betti curves. As predicted, as more edges are shuffled, the distribution of Betti curves converges to the pattern of the Random NM. In the forward filtration, the shape of Betti curves is not changed until $k = 30\%$ of the connections are randomised; even at that stage, the curve is shifted very slightly toward earlier filtration steps, but retains the same shape. This shows the robustness of the method to 'noise' from weak connections. Interestingly, this level, 30%, is the average proportion of zero connections found in *COBRE*. This demonstrates how, despite the stark difference in terms of numbers of missing connections, we still find the same cycles in both *COBRE* and *HCP*.

Further increasing the proportion of connections shuffled results in the emergence of higher-dimensional cycles. The latter are absent from the original matrix, but are expected to be present in random matrices of the same size. The shape of the Betti curves from *HCP* remains largely unchanged until the $k = 60\%$ level, where it starts to be overrun by a 'tsunami of randomness' (Figure Supp.B.23), after which there is a significant rise in the number of cycles in the randomised part of the filtration, and the structure converges to the Random NM.

# 4 Discussion

Our study of topological changes in schizophrenia utilises descriptors capable of capturing nuanced differences in connectivity patterns. Instead of focussing on how a disease, such as schizophrenia, affects individual regions, captured as deviations in brain morphometrics, we examined the connectivity patterns at multiple scales specified by the filtration steps of the order complex.

By using an ordered matrix instead of directly using the output matrix produced by the probabilistic fibre tracking algorithm (Figure 1), we ensured that the derived topological properties rely on the relative connections within a participant's brain and not on estimates of absolute fibre count. Using absolute fibre counts may have contributed to the variability of reports of schizophrenia-related brain alterations in previous studies, as mentioned by Wheeler et al. [Wheeler and Voineskos, 2014] and Howes et al. [Howes et al., 2023]. In contrast, using ordered connections, as was done here, resolves this issue and makes the comparison between different groups more reliable.

Investigating the ranking of connections within individuals allows us to examine the sequence in which connections are integrated into the subject's connectome. This individualized framework facilitates a subject-specific characterization of brain connectivity. Notably, despite inter-individual variability, connectomes exhibit a substantial number of shared topological features (cycles seen in both datasets). Many cycles emerged at consistent ranks across subjects, suggesting that their formation follows overarching principles of brain organization (Figure 4).

Differences between the schizophrenia and healthy control groups are evident both globally, via persistence landscapes (Figure 5), and locally, through sublandscape analysis (Figure 6). In schizophrenia, cycles exhibited later birth times and delayed deaths, consistent with the white matter disconnectivity hypothesis [Glahn et al., 2008, Ellison-Wright and Bullmore, 2009, Fornito et al., 2009, Schmitt et al., 2011, Vitolo et al., 2017, Kelly et al., 2018]. Interestingly, the significantly different sublandscapes involved cycles containing regions previously implicated in schizophrenia, such as the *left* and *right precuneus*, *inferior parietal gyrus*, *superior temporal gyrus*, and *superior occipital gyrus*. We note that the cycles with significantly different persistence landscapes are always found in subpopulations, never in all participants, however, all schizophrenia participants possess at least one of the significant cycles. This heterogeneity reflects the heterogeneity of the vast spectrum of symptoms. Future work involving larger groups of patients with schizophrenia will enable us to link specific mesoscale topological motifs to symptoms.

The recurrence of homology class representatives (and their birth and death times) across individuals in both the *COBRE* and *HCP* datasets (Figure 7), despite differences in scanning equipment, demonstrates that cycles are meaningful descriptors of white matter connectivity patterns. Each individual has a set of cycles and persistent bar codes which constitute a 'connectomic fingerprint'. These features could inform future experimental designs aimed at probing schizophrenia-related brain changes and serve as starting points for neuropathological investigations.

Persistent homology offers a novel perspective on brain connectivity by focusing on cycles—topological holes that persist across filtration steps. This enables us to indicate which sets of brain regions, and not just single regions, exhibit different properties between the two groups. This is particularly well-suited to studying white matter nerve bundles, which inherently span multiple regions. The schizophrenia literature tends to report only which bundles are affected [Kelly et al., 2018] or that the bundles change with age [Cropley et al., 2017]; whereas they rarely specify the precise inter-regional connections involved. Our method enables us to localise the alterations to subsegments of tracts, thereby providing a more precise anatomical characterisation of the affected pathways, rather than reporting only whole tract abnormalities.

Although our approach, by design, is robust to monotonic transformations, which mitigates some of the dependency on the quality of the connectivity matrix and, in turn, its dependency on choices of scanning hardware, scanning protocol, acquisition parameters, and preprocessing steps, etc., potential sources of error remain. Further investigation of the susceptibility of our approach to the preprocessing steps would be useful, but would require the availability of datasets where scans have been performed on the same individual with different scanner settings and preprocessing steps, ideally on the same day. See Supplementary Section B.13 for a more detailed discussion on strengths, limitations and future directions.

To summarise, we have presented a novel approach for producing detailed connectivity

profiles of the human brain, which could serve as future neuroimaging-based biomarkers for schizophrenia and other neurological diseases. As an overarching future direction, we aim to establish a DTI-based topological connectomic fingerprint by extending our investigation to larger healthy populations. In the context of the diseased populations, particularly those with schizophrenia, our immediate future directions include to test its reliability and validity as a biomarker, by testing the link between this connectomic fingerprint with the disorder's phenotypic and/or genetic markers, and by applying the methods in different schizophrenia subpopulations (e.g., early-onset, unmedicated, treatment-resistance patients) to add a new connectomic perspective on the disorder's heterogeneity.

## Acknowledgements

CM was supported by the Einstein Stiftung Berlin (A-2020-613).

Data used in the preparation of this article were obtained from the SchizConnect database (http://schizconnect.org). Data were provided (in part) by the Human Connectome Project, WU-Minn Consortium (Principal Investigators: David Van Essen and Kamil Ugurbil; 1U54MH091657) funded by the 16 NIH Institutes and Centers that support the NIH Blueprint for Neuroscience Research, and by the McDonnell Center for Systems Neuroscience at Washington University.

All the code was implemented in the Julia [Bezanson et al., 2017] programming language and the persistence homology calculations were performed using the *Eirene* library [Henselman and Ghrist, 2017], supported by the "PersistenceLandscapes.jl" [Dmitruk et al., 2021, Bubenik and Dłotko, 2017] and "DrWatson.jl" [Datseris et al., 2020] libraries.

## References


[Aine et al., 2017] Aine, C. J., Bockholt, H. J., Bustillo, J. R., Cañive, J. M., Caprihan, A., Gasparovic, C., Hanlon, F. M., Houck, J. M., Jung, R. E., Lauriello, J., Liu, J., Mayer, A. R., Perrone-Bizzozero, N. I., Posse, S., Stephen, J. M., Turner, J. A., Clark, V. P., and Calhoun, V. D. (2017). Multimodal Neuroimaging in Schizophrenia: Description and Dissemination. *Neuroinformatics*, 15(4):343–364.

[Alexander-Bloch et al., 2013] Alexander-Bloch, A. F., Vértes, P. E., Stidd, R., Lalonde, F., Clasen, L., Rapoport, J., Giedd, J., Bullmore, E. T., and Gogtay, N. (2013). The Anatomical Distance of Functional Connections Predicts Brain Network Topology in Health and Schizophrenia. *Cerebral Cortex*, 23(1):127–138.

[Ambrosen et al., 2020] Ambrosen, K. S., Eskildsen, S. F., Hinne, M., Krug, K., Lundell, H., Schmidt, M. N., van Gerven, M. A. J., Mørup, M., and Dyrby, T. B. (2020). Validation of structural brain connectivity networks: The impact of scanning parameters. *NeuroImage*, 204:116207.

[Anderson et al., 2018] Anderson, K. L., Anderson, J. S., Palande, S., and Wang, B. (2018). Topological Data Analysis of Functional MRI Connectivity in Time and Space Domains. *Connect Neuroimaging*.

[Behrens et al., 2007] Behrens, T., Johansen Berg, H., Jbabdi, S., Rushworth, M., and Woolrich, M. W. (2007). Probabilistic diffusion tractography with multiple fibre orientations: What can we gain? *NeuroImage*, 34(1):144–55.

[Bendich et al., 2016] Bendich, P., Marron, J. S., Miller, E., Pieloch, A., and Skwerer, S. (2016). Persistent Homology Analysis of Brain Artery Trees. *The Annals of Applied Statistics*, 10(1):198–218.

[Betzel and Bassett, 2017] Betzel, R. F. and Bassett, D. S. (2017). Multi-scale brain networks. *NeuroImage*, 160:73–83.

[Betzel and Bassett, 2018] Betzel, R. F. and Bassett, D. S. (2018). Specificity and robustness of long-distance connections in weighted, interareal connectomes. *Proceedings of the National Academy of Sciences*, 115(21):E4880–E4889.

[Bezanson et al., 2017] Bezanson, J., Edelman, A., Karpinski, S., and Shah, V. B. (2017). Julia: A fresh approach to numerical computing. *SIAM Review*, 59(1):65–98.

[Brett et al., 2002] Brett, M., Johnsrude, I. S., and Owen, A. M. (2002). The problem of functional localization in the human brain. *Nature Reviews Neuroscience*, 3(3):243–249.

[Brugger and Howes, 2017] Brugger, S. P. and Howes, O. D. (2017). Heterogeneity and Homogeneity of Regional Brain Structure in Schizophrenia: A Meta-analysis. *JAMA psychiatry*, 74(11):1104–1111.

[Bubenik, 2015] Bubenik, P. (2015). Statistical topological data analysis using persistence landscapes. *Journal of Machine Learning Research*, 16:77–102.

[Bubenik and Dłotko, 2017] Bubenik, P. and Dłotko, P. (2017). A persistence landscapes toolbox for topological statistics. *Journal of Symbolic Computation*, 78:91–114.

[Bullmore and Sporns, 2009] Bullmore, E. and Sporns, O. (2009). Complex brain networks: Graph theoretical analysis of structural and functional systems. *Nature Reviews Neuroscience*, 10(3):186–198.

[Bullmore and Sporns, 2012] Bullmore, E. and Sporns, O. (2012). The economy of brain network organization. *Nature Reviews Neuroscience*, 13(5):336–349.

[Caan, 2016] Caan, M. W. A. (2016). DTI Analysis Methods: Fibre Tracking and Connectivity. In Van Hecke, W., Emsell, L., and Sunaert, S., editors, *Diffusion Tensor Imaging*, pages 205–228. Springer New York, New York, NY.

[Canu et al., 2015] Canu, E., Agosta, F., and Filippi, M. (2015). A selective review of structural connectivity abnormalities of schizophrenic patients at different stages of the disease. *Schizophrenia Research*, 161(1):19–28.

[Cao et al., 2003] Cao, Y., Whalen, S., Huang, J., Berger, K. L., and DeLano, M. C. (2003). Asymmetry of subinsular anisotropy by in vivo diffusion tensor imaging. *Human Brain Mapping*, 20(2):82–90.

[Caputi et al., 2021] Caputi, L., Pidnebesna, A., and Hlinka, J. (2021). Promises and pitfalls of topological data analysis for brain connectivity analysis. *NeuroImage*, 238:118245.

[Cetin et al., 2014] Cetin, M. S., Christensen, F., Abbott, C. C., Stephen, J. M., Mayer, A. R., Cañive, J. M., Bustillo, J. R., Pearlson, G. D., and Calhoun, V. D. (2014). Thalamus and posterior temporal lobe show greater inter-network connectivity at rest and across sensory paradigms in schizophrenia. *NeuroImage*, 97:117–126.

[Chung and Cannon, 2015] Chung, Y. and Cannon, T. D. (2015). Brain Imaging During the Transition from Psychosis Prodrome to Schizophrenia. *Journal of Nervous & Mental Disease*, 203(5):336–341.

[Cropley et al., 2017] Cropley, V. L., Klauser, P., Lenroot, R. K., Bruggemann, J., Sundram, S., Bousman, C., Pereira, A., Di Biase, M. A., Weickert, T. W., Weickert, C. S., Pantelis, C., and Zalesky, A. (2017). Accelerated Gray and White Matter Deterioration With Age in Schizophrenia. *American Journal of Psychiatry*, 174(3):286–295.

[Datseris et al., 2020] Datseris, G., Isensee, J., Pech, S., and Gál, T. (2020). DrWatson: The perfect sidekick for your scientific inquiries. *Journal of Open Source Software*, 5(54):2673.

[Dimulescu et al., 2021] Dimulescu, C., Gareayaghi, S., Kamp, F., Fromm, S., Obermayer, K., and Metzner, C. (2021). Structural differences between healthy subjects and patients with schizophrenia and schizoaffective disorder: A graph and control theoretical perspective. Preprint, Psychiatry and Clinical Psychology.

[Dmitruk et al., 2021] Dmitruk, E., Metzner, C., Steuber, V., and Kadir, S. (2021). Larger inter-individual variability of large-scale brain organization in schizophrenia revealed by topological data analysis. *Journal of Computational Neuroscience*, 49(1):S22–S24.

[Drakesmith et al., 2015] Drakesmith, M., Caeyenberghs, K., Dutt, A., Lewis, G., David, A., and Jones, D. (2015). Overcoming the effects of false positives and threshold bias in graph theoretical analyses of neuroimaging data. *Neuroimage*, 118:313–333.

[Ellis et al., 2019] Ellis, C. T., Lesnick, M., Henselman-Petrusek, G., Keller, B., and Cohen, J. D. (2019). Feasibility of topological data analysis for event-related fMRI. *Network Neuroscience*, 3(3):695–706.

[Ellis and Klein, 2014] Ellis, S. P. and Klein, A. (2014). Describing high-order statistical dependence using "concurrence topology," with application to functional MRI brain data. *Homology, Homotopy and Applications*, 16(1):245–264.

[Ellison-Wright and Bullmore, 2009] Ellison-Wright, I. and Bullmore, E. (2009). Meta-analysis of diffusion tensor imaging studies in schizophrenia. *Schizophrenia Research*, 108(1-3):3–10.

[Evans et al., 1992] Evans, A. C., Collins, D., and Milner, B. (1992). An MRI-based stereotactic atlas from 250 young normal subjects. *The Society for Neuroscience Abstracts*.

[Faskowitz et al., 2022] Faskowitz, J., Betzel, R. F., and Sporns, O. (2022). Edges in brain networks: Contributions to models of structure and function. *Network Neuroscience*, 6(1):1–28.

[Faskowitz et al., 2020] Faskowitz, J., Esfahlani, F. Z., Jo, Y., Sporns, O., and Betzel, R. F. (2020). Edge-centric functional network representations of human cerebral cortex reveal overlapping system-level architecture. *Nature Neuroscience*, 23(12):1644–1654.

[Fornito et al., 2011] Fornito, A., Yoon, J., Zalesky, A., Bullmore, E. T., and Carter, C. S. (2011). General and Specific Functional Connectivity Disturbances in First-Episode Schizophrenia During Cognitive Control Performance. *Biological Psychiatry*, 70(1):64–72.

[Fornito et al., 2009] Fornito, A., Yücel, M., Patti, J., Wood, S. J., and Pantelis, C. (2009). Mapping grey matter reductions in schizophrenia: An anatomical likelihood estimation analysis of voxel-based morphometry studies. *Schizophrenia Research*, 108(1):104–113.

[Fornito et al., 2016] Fornito, A., Zalesky, A., and Bullmore, E. T. (2016). *Fundamentals of Brain Network Analysis*. Elsevier Science & Technology, San Diego.

[Fortea et al., 2021] Fortea, A., Batalla, A., Radua, J., van Eijndhoven, P., Baeza, I., Albajes-Eizagirre, A., Fusar-Poli, P., Castro-Fornieles, J., De la Serna, E., Luna, L. P., Carvalho, A. F., Vieta, E., and Sugranyes, G. (2021). Cortical gray matter reduction precedes transition to psychosis in individuals at clinical high-risk for psychosis: A voxel-based meta-analysis. *Schizophrenia Research*, 232:98–106.

[Fournier et al., 2020] Fournier, M., Scolamiero, M., Gholam-Rezaee, M. M., Cleusix, M., Jenni, R., Ferrari, C., Golay, P., Baumann, P. S., Cuenod, M., Conus, P., Do, K. Q., and Hess, K. (2020). Topology predicts long-term functional outcome in early psychosis. *Molecular Psychiatry*, pages 1–12.

[Gao et al., 2018] Gao, X., Zhang, W., Yao, L., Xiao, Y., Liu, L., Liu, J., Li, S., Tao, B., Shah, C., Gong, Q., Sweeney, J. A., and Lui, S. (2018). Association between structural and functional brain alterations in drug-free patients with schizophrenia: A multimodal meta-analysis. *Journal of Psychiatry and Neuroscience*, 43(2):131–142.

[Gao et al., 2023] Gao, Z., Xiao, Y., Zhu, F., Tao, B., Yu, W., and Lui, S. (2023). The whole-brain connectome landscape in patients with schizophrenia: A systematic review and meta-analysis of graph theoretical characteristics. *Neuroscience & Biobehavioral Reviews*, 148:105144.

[Giusti et al., 2015a] Giusti, C., Pastalkova, E., Curto, C., and Itskov, V. (2015a). Clique Topology Appendix. *Proceedings of the National Academy of Sciences*, 112(44):1–14.

[Giusti et al., 2015b] Giusti, C., Pastalkova, E., Curto, C., and Itskov, V. (2015b). Clique topology reveals intrinsic geometric structure in neural correlations. *Proceedings of the National Academy of Sciences*, 112(44):13455–13460.

[Glahn et al., 2008] Glahn, D. C., Laird, A. R., Ellison-Wright, I., Thelen, S. M., Robinson, J. L., Lancaster, J. L., Bullmore, E., and Fox, P. T. (2008). Meta-Analysis of Gray Matter Anomalies in Schizophrenia: Application of Anatomic Likelihood Estimation and Network Analysis. *Biological Psychiatry*, 64(9):774–781.

[Good et al., 2001] Good, C. D., Johnsrude, I., Ashburner, J., Henson, R. N. A., Friston, K. J., and Frackowiak, R. S. J. (2001). Cerebral Asymmetry and the Effects of Sex and Handedness on Brain Structure: A Voxel-Based Morphometric Analysis of 465 Normal Adult Human Brains. *NeuroImage*, 14(3):685–700.

[Gordon et al., 2017] Gordon, E. M., Laumann, T. O., Gilmore, A. W., Newbold, D. J., Greene, D. J., Berg, J. J., Ortega, M., Hoyt-Drazen, C., Gratton, C., Sun, H., Hampton, J. M., Coalson, R. S., Nguyen, A. L., McDermott, K. B., Shimony, J. S., Snyder, A. Z., Schlaggar, B. L., Petersen, S. E., Nelson, S. M., and Dosenbach, N. U. (2017). Precision Functional Mapping of Individual Human Brains. *Neuron*, 95(4):791–807.e7.

[Gutierrez et al., 2020] Gutierrez, C. E., Skibbe, H., Nakae, K., Tsukada, H., Lienard, J., Watakabe, A., Hata, J., Reisert, M., Woodward, A., Yamaguchi, Y., Yamamori, T., Okano, H., Ishii, S., and Doya, K. (2020). Optimization and validation of diffusion MRI-based fiber tracking with neural tracer data as a reference. *Scientific Reports*, 10(1):21285.

[Hadley et al., 2016] Hadley, J. A., Kraguljac, N. V., White, D. M., Ver Hoef, L., Tabora, J., and Lahti, A. C. (2016). Change in brain network topology as a function of treatment response in schizophrenia: A longitudinal resting-state fMRI study using graph theory. *npj Schizophrenia*, 2(1):1–7.

[Haukvik et al., 2013] Haukvik, U. K., Hartberg, C. B., and Agartz, I. (2013). Schizophrenia–what does structural MRI show? *Tidsskrift for Den Norske Laegeforening: Tidsskrift for Praktisk Medicin, Ny Raekke*, 133(8):850–853.

[Henselman and Ghrist, 2017] Henselman, G. and Ghrist, R. (2017). Matroid Filtrations and Computational Persistent Homology. *arXiv:1606.00199 [math]*.

[Hernández et al., 2013] Hernández, M., Guerrero, G. D., Cecilia, J. M., García, J. M., Inuggi, A., Jbabdi, S., Behrens, T. E. J., and Sotiropoulos, S. N. (2013). Accelerating Fibre Orientation Estimation from Diffusion Weighted Magnetic Resonance Imaging Using GPUs. *PLOS ONE*, 8(4):e61892.

[Hervé et al., 2013] Hervé, P.-Y., Zago, L., Petit, L., Mazoyer, B., and Tzourio-Mazoyer, N. (2013). Revisiting human hemispheric specialization with neuroimaging. *Trends in Cognitive Sciences*, 17(2):69–80.

[Ho et al., 2017] Ho, N. F., Li, Z., Ji, F., Wang, M., Kuswanto, C. N., Sum, M. Y., Tng, H. Y., Sitoh, Y. Y., Sim, K., and Zhou, J. (2017). Hemispheric lateralization abnormalities of the white matter microstructure in patients with schizophrenia and bipolar disorder. *Journal of Psychiatry and Neuroscience*, 42(4):242–251.

[Howes et al., 2023] Howes, O. D., Cummings, C., Chapman, G. E., and Shatalina, E. (2023). Neuroimaging in schizophrenia: An overview of findings and their implications for synaptic changes. *Neuropsychopharmacology*, 48(1):151–167.

[Jenkinson et al., 2012] Jenkinson, M., Beckmann, C. F., Behrens, T. E. J., Woolrich, M. W., and Smith, S. M. (2012). FSL. *NeuroImage*, 62(2):782–790.

[Kahle, 2013] Kahle, M. (2013). Topology of random simplicial complexes: A survey.

[Kanari et al., 2018] Kanari, L., Dłotko, P., Scolamiero, M., Levi, R., Shillcock, J., Hess, K., and Markram, H. (2018). A Topological Representation of Branching Neuronal Morphologies. *Neuroinformatics*, 16(1):3–13.

[Kelly et al., 2018] Kelly, S., Jahanshad, N., Zalesky, A., Kochunov, P., Agartz, I., Alloza, C., Andreassen, O. A., Arango, C., Banaj, N., Bouix, S., Bousman, C. A., Brouwer, R. M., Bruggemann, J., Bustillo, J., Cahn, W., Calhoun, V., Cannon, D., Carr, V., Catts, S., Chen, J., Chen, J.-x., Chen, X., Chiapponi, C., Cho, K. K., Ciullo, V., Corvin, A. S., Crespo-Facorro, B., Cropley, V., De Rossi, P., Diaz-Caneja, C. M., Dickie, E. W., Ehrlich, S., Fan, F.-m., Faskowitz, J., Fatouros-Bergman, H., Flyckt, L., Ford, J. M., Fouche, J.-P., Fukunaga, M., Gill, M., Glahn, D. C., Gollub, R., Goudzwaard, E. D., Guo, H., Gur, R. E., Gur, R. C., Gurholt, T. P., Hashimoto, R., Hatton, S. N., Henskens, F. A., Hibar, D. P., Hickie, I. B., Hong, L. E., Horacek, J., Howells, F. M., Hulshoff Pol, H. E., Hyde, C. L., Isaev, D., Jablensky, A., Jansen, P. R., Janssen, J., Jönsson, E. G., Jung, L. A., Kahn, R. S., Kikinis, Z., Liu, K., Klauser, P., Knöchel, C., Kubicki, M., Lagopoulos, J., Langen, C., Lawrie, S., Lenroot, R. K., Lim, K. O., Lopez-Jaramillo, C., Lyall, A., Magnotta, V., Mandl, R. C. W., Mathalon, D. H., McCarley, R. W., McCarthy-Jones, S., McDonald, C., McEwen, S., McIntosh, A., Melicher, T., Mesholam-Gately, R. I., Michie, P. T., Mowry, B., Mueller, B. A., Newell, D. T., O'Donnell, P., Oertel-Knöchel, V., Oestreich, L., Paciga, S. A., Pantelis, C., Pasternak, O., Pearlson, G., Pellicano, G. R., Pereira, A., Pineda Zapata, J., Piras, F., Potkin, S. G., Preda, A., Rasser, P. E., Roalf, D. R., Roiz, R., Roos, A., Rotenberg, D., Satterthwaite, T. D., Savadjiev, P., Schall, U., Scott, R. J., Seal, M. L., Seidman, L. J., Shannon Weickert, C., Whelan, C. D., Shenton, M. E., Kwon, J. S., Spalletta, G., Spaniel, F., Sprooten, E., Stäblein, M., Stein, D. J., Sundram, S., Tan, Y., Tan, S., Tang, S., Temmingh, H. S., Westlye, L. T., Tønnesen, S., Tordesillas-Gutierrez, D., Doan, N. T., Vaidya, J., van Haren, N. E. M., Vargas, C. D., Vecchio, D., Velakoulis, D., Voineskos, A., Voyvodic, J. Q., Wang, Z., Wan, P., Wei, D., Weickert, T. W., Whalley, H., White, T., Whitford, T. J., Wojcik, J. D., Xiang, H., Xie, Z., Yamamori, H., Yang, F., Yao, N., Zhang, G., Zhao, J., van Erp, T. G. M., Turner, J., Thompson, P. M., and Donohoe, G. (2018). Widespread white matter microstructural differences in schizophrenia across 4322 individuals: Results from the ENIGMA Schizophrenia DTI Working Group. *Molecular Psychiatry*, 23(5):1261–1269.

[Konrad and Winterer, 2007] Konrad, A. and Winterer, G. (2007). Disturbed Structural Connectivity in Schizophrenia Primary Factor in Pathology or Epiphenomenon? *Schizophrenia Bulletin*, 34(1):72–92.

[Kuo and Pogue-Geile, 2019] Kuo, S. S. and Pogue-Geile, M. F. (2019). Variation in fourteen brain structure volumes in schizophrenia: A comprehensive meta-analysis of 246 studies. *Neuroscience & Biobehavioral Reviews*, 98:85–94.

[Lancaster et al., 2003] Lancaster, J. L., Kochunov, P. V., Thompson, P. M., Toga, A. W., and Fox, P. T. (2003). Asymmetry of the brain surface from deformation field analysis. *Human Brain Mapping*, 19(2):79–89.

[Lee et al., 2011] Lee, H., Chung, M. K., Kang, H., Kim, B. N., and Lee, D. S. (2011). Discriminative persistent homology of brain networks. *Proceedings - International Symposium on Biomedical Imaging*, pages 841–844.

[Li et al., 2015] Li, H., Tang, J., Chen, L., Liao, Y., Zhou, B., He, Y., Li, Z., Lv, L., Zeng, Y., and Chen, X. (2015). Reduced middle cingulate gyrus volume in late-onset schizophrenia in a Chinese Han population: A voxel-based structural MRI study. *Neuroscience Bulletin*, 31(5):626–627.

[Lord et al., 2016] Lord, L.-D., Expert, P., Fernandes, H. M., Petri, G., Van Hartevelt, T. J., Vaccarino, F., Deco, G., Turkheimer, F., and Kringelbach, M. L. (2016). Insights into Brain Architectures from the Homological Scaffolds of Functional Connectivity Networks. *Frontiers in Systems Neuroscience*, 10(November):1–14.

[Luvsannyam et al., 2022] Luvsannyam, E., Jain, M. S., Pormento, M. K. L., Siddiqui, H., Balagtas, A. R. A., Emuze, B. O., and Poprawski, T. (2022). Neurobiology of Schizophrenia: A Comprehensive Review. *Cureus*, 14(4):e23959.

[Maier-Hein et al., 2017] Maier-Hein, K. H., Neher, P. F., Houde, J.-C., Côté, M.-A., Garyfallidis, E., Zhong, J., Chamberland, M., Yeh, F.-C., Lin, Y.-C., Ji, Q., Reddick, W. E., Glass, J. O., Chen, D. Q., Feng, Y., Gao, C., Wu, Y., Ma, J., He, R., Li, Q., Westin, C.-F., Deslauriers-Gauthier, S., González, J. O. O., Paquette, M., St-Jean, S., Girard, G., Rheault, F., Sidhu, J., Tax, C. M. W., Guo, F., Mesri, H. Y., Dávid, S., Froeling, M., Heemskerk, A. M., Leemans, A., Boré, A., Pinsard, B., Bedetti, C., Desrosiers, M., Brambati, S., Doyon, J., Sarica, A., Vasta, R., Cerasa, A., Quattrone, A., Yeatman, J., Khan, A. R., Hodges, W., Alexander, S., Romascano, D., Barakovic, M., Auría, A., Esteban, O., Lemkaddem, A., Thiran, J.-P., Cetingul, H. E., Odry, B. L., Mailhe, B., Nadar, M. S., Pizzagalli, F., Prasad, G., Villalon-Reina, J. E., Galvis, J., Thompson, P. M., Requejo, F. D. S., Laguna, P. L., Lacerda, L. M., Barrett, R., Dell'Acqua, F., Catani, M., Petit, L., Caruyer, E., Daducci, A., Dyrby, T. B., Holland-Letz, T., Hilgetag, C. C., Stieltjes, B., and Descoteaux, M. (2017). The challenge of mapping the human connectome based on diffusion tractography. *Nature Communications*, 8:1349.

[Male et al., 2024] Male, A. G., Goudzwaard, E., Nakahara, S., Turner, J. A., Calhoun, V. D., Mueller, B. A., Lim, K. O., Bustillo, J. R., Belger, A., Voyvodic, J., O'Leary, D., Mathalon, D. H., Ford, J. M., Potkin, S. G., Preda, A., and van Erp, T. G. M. (2024). Structural white matter abnormalities in Schizophrenia and associations with neurocognitive performance and symptom severity. *Psychiatry Research: Neuroimaging*, 342:111843.

[Merritt et al., 2021] Merritt, K., Luque Laguna, P., Irfan, A., and David, A. S. (2021). Longitudinal Structural MRI Findings in Individuals at Genetic and Clinical High Risk for Psychosis: A Systematic Review. *Frontiers in Psychiatry*, 12:620401.

[Molina et al., 2008] Molina, V., Reig, S., Sanz, J., Palomo, T., Benito, C., Sarramea, F., Pascau, J., Sánchez, J., Martín-Loeches, M., Muñoz, F., and Desco, M. (2008). Differential clinical, structural and P300 parameters in schizophrenia patients resistant to conventional neuroleptics. *Progress in Neuro-Psychopharmacology and Biological Psychiatry*, 32(1):257–266.

[Oldham et al., 2022] Oldham, S., Fulcher, B. D., Aquino, K., Arnatkevičiūtė, A., Paquola, C., Shishegar, R., and Fornito, A. (2022). Modeling spatial, developmental, physiological, and topological constraints on human brain connectivity. *Science Advances*, 8(22):eabm6127.

[Osimo et al., 2019] Osimo, E. F., Beck, K., Reis Marques, T., and Howes, O. D. (2019). Synaptic loss in schizophrenia: A meta-analysis and systematic review of synaptic protein and mRNA measures. *Molecular Psychiatry*, 24(4):549–561.

[Otter et al., 2017] Otter, N., Porter, M. A., Tillmann, U., Grindrod, P., and Harrington, H. A. (2017). A roadmap for the computation of persistent homology. *EPJ Data Science*, 6(1).

[Ottet et al., 2013] Ottet, M.-C., Schaer, M., Debbané, M., Cammoun, L., Thiran, J.-P., and Eliez, S. (2013). Graph theory reveals dysconnected hubs in 22q11DS and altered nodal efficiency in patients with hallucinations. *Frontiers in Human Neuroscience*, 7.

[Petri et al., 2014] Petri, G., Expert, P., Turkheimer, F., Carhart-Harris, R., Nutt, D., Hellyer, P. J., and Vaccarino, F. (2014). Homological scaffolds of brain functional networks. *Journal of The Royal Society Interface*, 11(101):20140873.

[Phinyomark et al., 2017] Phinyomark, A., Ibanez-Marcelo, E., and Petri, G. (2017). Resting-State fMRI Functional Connectivity: Big Data Preprocessing Pipelines and Topological Data Analysis. *IEEE Transactions on Big Data*, 3(4):415–428.

[Ragland et al., 2009] Ragland, J. D., Laird, A. R., Ranganath, C., Blumenfeld, R. S., Gonzales, S. M., and Glahn, D. C. (2009). Prefrontal Activation Deficits During Episodic Memory in Schizophrenia. *American Journal of Psychiatry*, 166(8):863–874.

[Repple et al., 2023] Repple, J., Gruber, M., Mauritz, M., de Lange, S. C., Winter, N. R., Opel, N., Goltermann, J., Meinert, S., Grotegerd, D., Leehr, E. J., Enneking, V., Borgers, T., Klug, M., Lemke, H., Waltemate, L., Thiel, K., Winter, A., Breuer, F., Grumbach, P., Hofmann, H., Stein, F., Brosch, K., Ringwald, K. G., Pfarr, J., Thomas-Odenthal, F., Meller, T., Jansen, A., Nenadic, I., Redlich, R., Bauer, J., Kircher, T., Hahn, T., van den Heuvel, M., and Dannlowski, U. (2023). Shared and Specific Patterns of Structural Brain Connectivity Across Affective and Psychotic Disorders. *Biological Psychiatry*, 93(2):178–186.

[Reveley et al., 2015] Reveley, C., Seth, A. K., Pierpaoli, C., Silva, A. C., Yu, D., Saunders, R. C., Leopold, D. A., and Ye, F. Q. (2015). Superficial white matter fiber systems impede detection of long-range cortical connections in diffusion MR tractography. *Proceedings of the National Academy of Sciences of the United States of America*, 112(21):E2820–E2828.

[Revell et al., 2022] Revell, A. Y., Silva, A. B., Arnold, T. C., Stein, J. M., Das, S. R., Shinohara, R. T., Bassett, D. S., Litt, B., and Davis, K. A. (2022). A framework For brain atlases: Lessons from seizure dynamics. *NeuroImage*, 254:118986.

[Rolls et al., 2020] Rolls, E. T., Huang, C.-C., Lin, C.-P., Feng, J., and Joliot, M. (2020). Automated anatomical labelling atlas 3. *NeuroImage*, 206:116189.

[Rolls et al., 2015] Rolls, E. T., Joliot, M., and Tzourio-Mazoyer, N. (2015). Implementation of a new parcellation of the orbitofrontal cortex in the automated anatomical labeling atlas. *NeuroImage*, 122:1–5.

[Rosa et al., 2021] Rosa, P. G. P., Zugman, A., Cerqueira, C. T., Serpa, M. H., de Souza Duran, F. L., Zanetti, M. V., Bassitt, D. P., Elkis, H., Crippa, J. A. S., Sallet, P. C., Gattaz, W. F., Hallak, J. E. C., Louzã, M. R., Gadelha, A., Jackowski, A. P., Bressan, R. A., and Filho, G. B. (2021). Cortical surface abnormalities are different depending on the stage of schizophrenia: A cross-sectional vertexwise mega-analysis of thickness, area and gyrification. *Schizophrenia Research*, 236:104–114.

[Rubinov and Sporns, 2010] Rubinov, M. and Sporns, O. (2010). Complex network measures of brain connectivity: Uses and interpretations. *NeuroImage*, 52(3):1059–1069.

[Sambataro et al., 2010] Sambataro, F., Blasi, G., Fazio, L., Caforio, G., Taurisano, P., Romano, R., Di Giorgio, A., Gelao, B., Lo Bianco, L., Papazacharias, A., Popolizio, T., Nardini, M., and Bertolino, A. (2010). Treatment with Olanzapine is Associated with Modulation of the Default Mode Network in Patients with Schizophrenia. *Neuropsychopharmacology*, 35(4):904–912.

[Sasabayashi et al., 2021] Sasabayashi, D., Takahashi, T., Takayanagi, Y., and Suzuki, M. (2021). Anomalous brain gyrification patterns in major psychiatric disorders: A systematic review and transdiagnostic integration. *Translational Psychiatry*, 11(1):1–12.

[Schaefer et al., 2018] Schaefer, A., Kong, R., Gordon, E. M., Laumann, T. O., Zuo, X.-N., Holmes, A. J., Eickhoff, S. B., and Yeo, B. T. T. (2018). Local-Global Parcellation of the Human Cerebral Cortex from Intrinsic Functional Connectivity MRI. *Cerebral Cortex (New York, N.Y.: 1991)*, 28(9):3095–3114.

[Schmitt et al., 2011] Schmitt, A., Hasan, A., Gruber, O., and Falkai, P. (2011). Schizophrenia as a disorder of disconnectivity. *European Archives of Psychiatry and Clinical Neuroscience*, 261(Suppl 2):150–154.

[Shen et al., 2023] Shen, C.-L., Tsai, S.-J., Lin, C.-P., and Yang, A. C. (2023). Progressive brain abnormalities in schizophrenia across different illness periods: A structural and functional MRI study. *Schizophrenia*, 9(1):1–9.

[Singh et al., 2008] Singh, G., Memoli, F., Ishkhanov, T., Sapiro, G., Carlsson, G., and Ringach, D. L. (2008). Topological analysis of population activity in visual cortex. *Journal of Vision*, 8(2008):1–18.

[Sizemore et al., 2018] Sizemore, A., Giusti, C., Kahn, A., Vettel, J. M., Betzel, R. F., and Bassett, D. (2018). Cliques and cavities in human connectome. *Journal of Computational Neuroscience*, pages 115–145.

[Smith et al., 2004] Smith, S. M., Jenkinson, M., Woolrich, M. W., Beckmann, C. F., Behrens, T. E. J., Johansen-Berg, H., Bannister, P. R., De Luca, M., Drobnjak, I., Flitney, D. E., Niazy, R. K., Saunders, J., Vickers, J., Zhang, Y., De Stefano, N., Brady, J. M., and Matthews, P. M. (2004). Advances in functional and structural MR image analysis and implementation as FSL. *NeuroImage*, 23 Suppl 1:S208–219.

[Sotiropoulos et al., 2013] Sotiropoulos, S. N., Moeller, S., Jbabdi, S., Xu, J., Andersson, J. L., Auerbach, E. J., Yacoub, E., Feinberg, D., Setsompop, K., Wald, L. L., Behrens, T. E. J., Ugurbil, K., and Lenglet, C. (2013). Effects of image reconstruction on fiber orientation mapping from multichannel diffusion MRI: Reducing the noise floor using SENSE. *Magnetic Resonance in Medicine*, 70(6):1682–1689.

[Sporns, 2013] Sporns, O. (2013). Network attributes for segregation and integration in the human brain. *Current Opinion in Neurobiology*, 23(2):162–171.

[Stam and Reijneveld, 2007] Stam, C. J. and Reijneveld, J. C. (2007). Graph theoretical analysis of complex networks in the brain. *Nonlinear Biomedical Physics*, 1(1):3.

[Stolz et al., 2018] Stolz, B., Emerson, T., Nahkuri, S., Porter, M. A., and Harrington, H. A. (2018). Topological Data Analysis of Task-Based fMRI Data from Experiments on Schizophrenia. *arXiv:1809.08504v2*.

[Stolz et al., 2017] Stolz, B. J., Harrington, H. A., and Porter, M. A. (2017). Persistent homology of time-dependent functional networks constructed from coupled time series. *Chaos: An Interdisciplinary Journal of Nonlinear Science*, 27(4):047410.

[Sun et al., 2015] Sun, H., Lui, S., Yao, L., Deng, W., Xiao, Y., Zhang, W., Huang, X., Hu, J., Bi, F., Li, T., Sweeney, J. A., and Gong, Q. (2015). Two Patterns of White Matter Abnormalities in Medication-Naive Patients With First-Episode Schizophrenia Revealed by Diffusion Tensor Imaging and Cluster Analysis. *JAMA Psychiatry*, 72(7):678.

[Sun et al., 2017] Sun, Y., Chen, Y., Collinson, S. L., Bezerianos, A., and Sim, K. (2017). Reduced Hemispheric Asymmetry of Brain Anatomical Networks Is Linked to Schizophrenia: A Connectome Study. *Cerebral Cortex*, 27(1):602–615.

[Takao et al., 2011a] Takao, H., Abe, O., Yamasue, H., Aoki, S., Sasaki, H., Kasai, K., Yoshioka, N., and Ohtomo, K. (2011a). Gray and white matter asymmetries in healthy individuals aged 21-29 years: A voxel-based morphometry and diffusion tensor imaging study. *Human Brain Mapping*, 32(10):1762–1773.

[Takao et al., 2011b] Takao, H., Hayashi, N., and Ohtomo, K. (2011b). White matter asymmetry in healthy individuals: A diffusion tensor imaging study using tract-based spatial statistics. *Neuroscience*, 193:291–299.

[Thieleking et al., 2021] Thieleking, R., Zhang, R., Paerisch, M., Wirkner, K., Anwander, A., Beyer, F., Villringer, A., and Witte, A. V. (2021). Same Brain, Different Look?—The Impact of Scanner, Sequence and Preprocessing on Diffusion Imaging Outcome Parameters. *Journal of Clinical Medicine*, 10(21):4987.

[Thomas et al., 2014] Thomas, C., Ye, F. Q., Irfanoglu, M. O., Modi, P., Saleem, K. S., Leopold, D. A., and Pierpaoli, C. (2014). Anatomical accuracy of brain connections derived from diffusion MRI tractography is inherently limited. *Proceedings of the National Academy of Sciences of the United States of America*, 111(46):16574–16579.

[Toga and Thompson, 2003] Toga, A. W. and Thompson, P. M. (2003). Mapping brain asymmetry. *Nature Reviews Neuroscience*, 4(1):37–48.

[Tohid et al., 2015] Tohid, H., Faizan, M., and Faizan, U. (2015). Alterations of the occipital lobe in schizophrenia. *Neurosciences*, 20(3):213–224.

[Tzourio-Mazoyer et al., 2002] Tzourio-Mazoyer, N., Landeau, B., Papathanassiou, D., Crivello, F., Etard, O., Delcroix, N., Mazoyer, B., and Joliot, M. (2002). Automated Anatomical Labeling of Activations in SPM Using a Macroscopic Anatomical Parcellation of the MNI MRI Single-Subject Brain. *NeuroImage*, 15(1):273–289.

[Utevsky et al., 2014] Utevsky, A. V., Smith, D. V., and Huettel, S. A. (2014). Precuneus Is a Functional Core of the Default-Mode Network. *The Journal of Neuroscience*, 34(3):932–940.

[Van Den Heuvel and Sporns, 2013] Van Den Heuvel, M. P. and Sporns, O. (2013). Network hubs in the human brain. *Trends in Cognitive Sciences*, 17(12):683–696.

[Van Den Heuvel and Sporns, 2019] Van Den Heuvel, M. P. and Sporns, O. (2019). A cross-disorder connectome landscape of brain dysconnectivity. *Nature Reviews Neuroscience*, 20(7):435–446.

[van den Heuvel et al., 2013] van den Heuvel, M. P., Sporns, O., Collin, G., Scheewe, T., Mandl, R. C. W., Cahn, W., Goñi, J., Hulshoff Pol, H. E., and Kahn, R. S. (2013). Abnormal Rich Club Organization and Functional Brain Dynamics in Schizophrenia. *JAMA Psychiatry*, 70(8):783.

[van Erp et al., 2018] van Erp, T. G. M., Walton, E., Hibar, D. P., Schmaal, L., Jiang, W., Glahn, D. C., Pearlson, G. D., Yao, N., Fukunaga, M., Hashimoto, R., Okada, N., Yamamori, H., Bustillo, J. R., Clark, V. P., Agartz, I., Mueller, B. A., Cahn, W., de Zwarte, S. M. C., Hulshoff Pol, H. E., Kahn, R. S., Ophoff, R. A., van Haren, N. E. M., Andreassen, O. A., Dale, A. M., Doan, N. T., Gurholt, T. P., Hartberg, C. B., Haukvik, U. K., Jørgensen, K. N., Lagerberg, T. V., Melle, I., Westlye, L. T., Gruber, O., Kraemer, B., Richter, A., Zilles, D., Calhoun, V. D., Crespo-Facorro, B., Roiz-Santiañez, R., Tordesillas-Gutiérrez, D., Loughland, C., Carr, V. J., Catts, S., Cropley, V. L., Fullerton, J. M., Green, M. J., Henskens, F. A., Jablensky, A., Lenroot, R. K., Mowry, B. J., Michie, P. T., Pantelis, C., Quidé, Y., Schall, U., Scott, R. J., Cairns, M. J., Seal, M., Tooney, P. A., Rasser, P. E., Cooper, G., Shannon Weickert, C., Weickert, T. W., Morris, D. W., Hong, E., Kochunov, P., Beard, L. M., Gur, R. E., Gur, R. C., Satterthwaite, T. D., Wolf, D. H., Belger, A., Brown, G. G., Ford, J. M., Macciardi, F., Mathalon, D. H., O'Leary, D. S., Potkin, S. G., Preda, A., Voyvodic, J., Lim, K. O., McEwen, S., Yang, F., Tan, Y., Tan, S., Wang, Z., Fan, F., Chen, J., Xiang, H., Tang, S., Guo, H., Wan, P., Wei, D., Bockholt, H. J., Ehrlich, S., Wolthusen, R. P. F., King, M. D., Shoemaker, J. M., Sponheim, S. R., De Haan, L., Koenders, L., Machielsen, M. W., van Amelsvoort, T., Veltman, D. J., Assogna, F., Banaj, N., de Rossi, P., Iorio, M., Piras, F., Spalletta, G., McKenna, P. J., Pomarol-Clotet, E., Salvador, R., Corvin, A., Donohoe, G., Kelly, S., Whelan, C. D., Dickie, E. W., Rotenberg, D., Voineskos, A. N., Ciufolini, S., Radua, J., Dazzan, P., Murray, R., Reis Marques, T., Simmons, A., Borgwardt, S., Egloff, L., Harrisberger, F., Riecher-Rössler, A., Smieskova, R., Alpert, K. I., Wang, L., Jönsson, E. G., Koops, S., Sommer, I. E. C., Bertolino, A., Bonvino, A., Di Giorgio, A., Neilson, E., Mayer, A. R., Stephen, J. M., Kwon, J. S., Yun, J.-Y., Cannon, D. M., McDonald, C., Lebedeva, I., Tomyshev, A. S., Akhadov, T., Kaleda, V., Fatouros-Bergman, H., Flyckt, L., Karolinska Schizophrenia Project, Busatto, G. F., Rosa, P. G. P., Serpa, M. H.,

Zanetti, M. V., Hoschl, C., Skoch, A., Spaniel, F., Tomecek, D., Hagenaars, S. P., McIntosh, A. M., Whalley, H. C., Lawrie, S. M., Knöchel, C., Oertel-Knöchel, V., Stäblein, M., Howells, F. M., Stein, D. J., Temmingh, H. S., Uhlmann, A., Lopez-Jaramillo, C., Dima, D., McMahon, A., Faskowitz, J. I., Gutman, B. A., Jahanshad, N., Thompson, P. M., and Turner, J. A. (2018). Cortical Brain Abnormalities in 4474 Individuals With Schizophrenia and 5098 Control Subjects via the Enhancing Neuro Imaging Genetics Through Meta Analysis (ENIGMA) Consortium. *Biological Psychiatry*, 84(9):644–654.

[Van Essen et al., 2012] Van Essen, D. C., Ugurbil, K., Auerbach, E., Barch, D., Behrens, T. E. J., Bucholz, R., Chang, A., Chen, L., Corbetta, M., Curtiss, S. W., Della Penna, S., Feinberg, D., Glasser, M. F., Harel, N., Heath, A. C., Larson-Prior, L., Marcus, D., Michalareas, G., Moeller, S., Oostenveld, R., Petersen, S. E., Prior, F., Schlaggar, B. L., Smith, S. M., Snyder, A. Z., Xu, J., Yacoub, E., and WU-Minn HCP Consortium (2012). The Human Connectome Project: A data acquisition perspective. *NeuroImage*, 62(4):2222–2231.

[Vita et al., 2012] Vita, A., De Peri, L., Deste, G., and Sacchetti, E. (2012). Progressive loss of cortical gray matter in schizophrenia: A meta-analysis and meta-regression of longitudinal MRI studies. *Translational Psychiatry*, 2(11):e190–e190.

[Vitolo et al., 2017] Vitolo, E., Tatu, M. K., Pignolo, C., Cauda, F., Costa, T., Ando', A., and Zennaro, A. (2017). White matter and schizophrenia: A meta-analysis of voxel-based morphometry and diffusion tensor imaging studies. *Psychiatry Research: Neuroimaging*, 270:8–21.

[Ward, 1963] Ward, J. (1963). Hierarchical Grouping to Optimize an Objective Function. *Journal of the American Statistical Association*, 58(301):236–244.

[Watkins et al., 2001] Watkins, K. E., Paus, T., Lerch, J. P., Zijdenbos, A., Collins, D. L., Neelin, P., Taylor, J., Worsley, K. J., and Evans, A. C. (2001). Structural asymmetries in the human brain: A voxel-based statistical analysis of 142 MRI scans. *Cerebral Cortex (New York, N.Y.: 1991)*, 11(9):868–877.

[Watson et al., 1988] Watson, D., Clark, L. A., and Tellegen, A. (1988). Development and validation of brief measures of positive and negative affect: The PANAS scales. *Journal of Personality and Social Psychology*, 54(6):1063–1070.

[Wheeler and Voineskos, 2014] Wheeler, A. L. and Voineskos, A. N. (2014). A review of structural neuroimaging in schizophrenia: From connectivity to connectomics. *Frontiers in Human Neuroscience*, 8.

[Witthaus et al., 2008] Witthaus, H., Brune, M., Kaufmann, C., Bohner, G., Ozgurdal, S., Gudlowski, Y., Heinz, A., Klingebiel, R., and Juckel, G. (2008). White matter abnormalities in subjects at ultra high-risk for schizophrenia and first-episode schizophrenic patients. *Schizophrenia Research*, 102(1-3):141–149.

[Yeo et al., 2011] Yeo, B. T. T., Krienen, F. M., Sepulcre, J., Sabuncu, M. R., Lashkari, D., Hollinshead, M., Roffman, J. L., Smoller, J. W., Zöllei, L., Polimeni, J. R., Fischl, B., Liu, H., and Buckner, R. L. (2011). The organization of the human cerebral cortex estimated by intrinsic functional connectivity. *Journal of Neurophysiology*, 106(3):1125–1165.

[Zalesky et al., 2011] Zalesky, A., Fornito, A., Seal, M. L., Cocchi, L., Westin, C.-F., Bullmore, E. T., Egan, G. F., and Pantelis, C. (2011). Disrupted Axonal Fiber Connectivity in Schizophrenia. *Biological Psychiatry*, 69(1):80–89.

[Zevon and Tellegen, 1982] Zevon, M. A. and Tellegen, A. (1982). The structure of mood change: An idiographic/nomothetic analysis. *Journal of Personality and Social Psychology*, 43(1):111–122.

[Zhang et al., 2023] Zhang, W., Xia, S., Tang, X., Zhang, X., Liang, D., and Wang, Y. (2023). Topological analysis of functional connectivity in Parkinson's disease. *Frontiers in Neuroscience*, 17:1236128.

[Zhao et al., 2018] Zhao, H., Gan, C., Rouditchenko, A., Vondrick, C., McDermott, J. H., and Torralba, A. (2018). The Sound of Pixels. *ECCV*.

[Zomorodian and Carlsson, 2005] Zomorodian, A. and Carlsson, G. (2005). Computing Persistent Homology. *Discrete & Computational Geometry*, 33(2):249–274.